Bulletin of Volcanology

Timescales and mechanisms of paroxysm initiation at Stromboli volcano, Aeolian islands, Italy

--Manuscript Draft--

Manuscript Number:	BUVO-D-21-00040R1
Full Title:	Timescales and mechanisms of paroxysm initiation at Stromboli volcano, Aeolian islands, Italy
Article Type:	Research Article
Corresponding Author:	Michel Pichavant ISTO-CNRS FRANCE
Corresponding Author Secondary Information:	
Order of Authors:	Michel Pichavant
	Ida Di Carlo
	Massimo Pompilio
	Nolwenn Le Gall
Funding Information:	Labex — Dr. Michel Pichavant Dr Ida Di Carlo
	Istituto Nazionale di Geofisica e Vulcanologia — Dr Massimo Pompilio
	Natural Environment Research Council — Dr Nolwenn Le Gall

Abstract:

New textural and petrological data are presented on products from 5 Stromboli paroxysms including the two from 2019 and three historical eruptions. The data are used to constrain timescales associated with the initiation of paroxysms and to examine current models for their triggering. Samples were collected from the deposits and a subset selected for mineral separation and petrological and textural characterization. Minerals and glasses were imaged by scanning electron microscopy (SEM) and both chemical compositions and zonations were analysed by electron microprobe. Trace elements in olivine were also determined. Vesicle number densities (N v), vesicularities (V) and vesicle sizes (D) were measured by X-ray microCT techniques. The data were systematically compared with results of experiments simulating, on the one hand, ascent, vesiculation, degassing and crystallization of LP (low-porphyricity) magmas and, on the other hand, interaction between LP and HP (high-porphyricity) magmas . Paroxysm samples are mixed and include portions representative of both LP and HP magmas. They host in variable proportions minerals and glasses texturally and compositionally typical of these two magma types. Small but systematic variations in matrix glass compositions are found between eruptions. All samples host a population of vesicles ranging from < 15 to > 1000 µm in D and whose size distributions follow mixed exponential to power law distributions. Vesicularities are high (75% on average) and vesicle number densities range from 10 2 -10 3 to 10 3 -10 4 mm -3 . Using experimental calibrations, the textural data suggest average LP magma ascent rates of 1-2 m/s (i.e., ~1.5 hour from 7 to 1.5 km depth), much higher than most geophysical estimates. The correlation between ascent rate and textures demonstrates systematic variations between eruptions, the most energetic (1930) being associated with the highest ascent rate (~2 m/s). Widths of plagioclase reaction zones indicate that LP and HP magmas interacted for a maximum a few hours before eruption. Olivine reaction also implies durations of a few hours for LP-HP interaction and is followed by crystallization for 20 hours in the HP magma. Our results stress the fast ascent of LP magmas from their storage region and their short residence times at shallow levels before being erupted. They clarify the respective roles of the deep and shallow feeding system in the initiation of paroxysms at Stromboli. The magma blob model offers the most promising perspectives toward an integrated model of paroxysm initiation at Stromboli.

Response to Reviewers:	Editor 1. Both reviewers also stress that a more detailed description of the origin of paroxysms (reviewer 1) should be provided or of alternate mechanisms (reviewer 2) should be discussed in the main text. See the reviewer's comments and our answers below 2. Reviewer 1 also suggests to add more details on how a well designed monitoring system could be envision based on the need to combine petrological evidence and geophysical records and the likehood of paroxysms being initiated at the deep crustal level. This section has been rewritten along the direction suggested by this reviewer (see below) 3. Reviever 1 would also like that the details on mineral structure to be included in the main text since their crucial impact on the reader's understanding of the crystallisation associated to the magma ascent. See answer to reviewer 1 below Reviewer 1 1. Interpretations are also made regarding potential triggers of paroxysms, and here I felt that interpretations were not conclusively supported by the data. In the section 'Implications for paroxysm triggering mechanisms', it is first observed that paroxysms are commonly preceded for days or weeks by heightened activity, either in the form of elevated gas flux and increased Strombolian activity (e.g. 2019 events) or effusive eruptions (e.g. 2003; 2007). This is followed by the suggestion of a gas driven mechanism of internal overpressurisation of the LP magma body as the trigger of paroxysms. I struggle to see how gas-driven overpressure and rapid magma ascent from the LP reservoir can be achieved following episodes of increased magma flux from the same magmatic system. Reading through the observations presented here, I wonder whether an alternative scenario may be worth considering, in which rapid evacuation of the shallow/HP magma reservoir destabilises the deeper/LP reservoir, initiating the rapid ascent recorded by petrological data here. Such a scenario would allow 'normal' recharge by LP magmas into the HP reservoir (as recorded by plagioclase zoning, etc) to be punctuated by these rarer paroxysms. Heightened activity leading up to paroxysms may result from elevated recharge rates from the LP reservoir driving increased magma output or from extrinsic factors such as dyking episodes. Given the connectivity between deep and shallow reservoirs, rapid loss of volume from the upper reservoir may destabilise the lower LP magma, either through a reduction in confining pressure or potentially changes in magma buoyancy (something like how a geyser works), initiating rapid ascent and paroxysm initiation. Such a scenario reconciles the petrological data presented here and by previous authors with the geophysical observations by groups like Calvari et al. I am not intimately familiar with Stromboli, so maybe there is key evidence that I have overlooked, however such a scenario certainly fits with my wider observations that the balance necessary for persistent volcanic activity like that at Stromboli is difficult to maintain. Although the aim of the paper is not to present a new model of paroxysm initiation, the suggestion made by this reviewer has been largely followed resulting in what is basically a new and expanded section "Paroxysm triggering mechanisms" 2. The authors offer recommendations for monitoring of Stromboli, and these support the development of techniques to monitor processes occurring at mid-deep crustal levels. Parts of this section ('Implications for monitoring') could be reworded to suggest development of a holistic monitoring program that looks at the magmatic system as a whole, from deep crustal levels to the surface. This section has been rewritten in the direction suggested Minor Comments: a. The 1930 and 16th century dates of the historical eruptions examined should be mentioned early in the introduction. Corrected in the revised version b. In the 'eruptions and samples section', details of petrology and magma ascent are explained for the 1930 and 16th century eruptions, but are not given for the 2019 eruptions. I guess there is less literature available for these most recent events, but it would still be interesting to know if the petrology differs amongst the two 2019 events and between them and earlier eruptions. The 1930, undated and 16th century eruptions have been previously investigated and the paper refers to those studies. In contrast, the 2019 products have started to be investigated more recently. Data presented in the paper contribute to the petrological

characterization of those recent products. However, our study is not aimed at systematically comparing the 2019 and the historical paroxysms. The “Mineralogical characteristics of LP magmas” section in the Supplementary Material is just an update and is not intended to detail the mineralogical characteristics of LP magmas. This has been clarified in the main text (“Mineral phases” section) and also in the Supplementary Material (introduction of the “Mineralogical characteristics of LP magmas” section).
c. The term ‘golden pumices’ is used, however is not clearly defined. Are these the same as LP magmas?
Golden pumice is used conveniently to define LP magma products. This is now made clear in the text (section “Methods”)
d. It is a shame that details on mineral textures have had to be included as supplementary material in order to keep this manuscript within the word and figure limits prescribed by the journal. The section ‘Ascent related crystallisation’ relies heavily on this information. I wonder if a short description of the mineral types relevant to this section of the text could be included in the main body of the manuscript.
Natural mineral types relevant to the discussion of “Ascent related crystallization” (third part of the section) are referenced to SEM pictures grouped in Fig. S4. The textures are also detailed further in the figure captions and in the “Mineralogical characteristics of LP magmas” section of the Supplementary Material. These textures constrain the temperature gradient during LP magma ascent which is less important as a topic than timescales. Therefore, there is no obvious reason why more emphasis should be placed on these mineralogical details
e. The authors recognise a relationship from experimental data between the reaction rim width in plagioclase (dplag) and interaction time between HP and LP magmas> This is then used to infer interaction times of hours, given the observation that dplag rarely exceeds 100 μm in natural samples. Time vs. dplag is plotted below from data in Table 2. Significant variation is apparent in dplag at t ~100 mins (33- 79 μm). A slower growth rate could be inferred from this, however even rapid interaction times of hours are required. If anything discussion of this variability, which is not presented by the authors at the moment, actually reinforces the overall interpretation that is made – i.e. interaction between shallow and deep magmas is limited to hours at most during paroxysm eruptions.
To account for the relative dispersion of the data noted by this reviewer, calculations have been carried out (100 μm reaction widths) by removing respectively either the minimum (R6-2) or the maximum point (R4-5, Table 2) from the power law regression. Results differ in detail compared to when all points are used for the regression (2.3 and 13.7 h vs. 5.5 h) but timescales are kept within a range of hours. This has been added to the text.
f. Does Fig. 4b show the same crystal as Fig. 4a? If so, the scale must be different? It would be useful to clarify this.
The captions to Fig. 4 have been slightly modified to clarify this problem
g. Figure 11a: The text refers to ‘geophysical’ and ‘petrological’ estimates of ‘u’, but it is unclear which are which in Fig. 11a. Maybe the geophysical and petrological estimates could be discriminated by symbol.
Different symbol colors are now used to distinguish between geophysical/volcanological and petrological estimates in this figure

Reviewer2
1. My comments are in the attached pdf document and mainly concern some clarification about the protocol used for the interaction experiments as well as image analysis and quantification of vesicle textures:
- Not the petrological model from Viccaro et al. 2021, Sci Reports, which invokes shallow dynamics based on Li enrichment in plagioclase, supported by tiltmeters data
This comment has been considered but later in the Discussion
- not all paroxysms have been preceded by effusive activity
This comment has also been considered in the Discussion (new section “Implications for paroxysm eruption triggering”)
- previous
added to the revised text
- what is the source of these data?
These data come from our own observations (added to the revised text)
- this is not in the references
Corrected in the revised text

	- what is the source of these data? See answer above - can you briefly specify what type of primitive end member are you referring to? Primitive here refers to the bulk rock chemistry and mineralogical characteristics (olivine and clinopyroxene compositions and textural types) of the undated eruption sample. The text has been slightly modified - In addition, could you add that golden pumices refer to LP magma and scoriae to HP magma? This has been specified in the revised text - Have you used two samples from Bertagnini et al 2011 as indicated in Table S1? Table S1 makes clear that both samples from Bertagnini et al. (2011) and new samples were studied - Please refer also to the pictures and description of mineral types in the Supplementary material, otherwise this part is not easy to follow References to pictures of mineral textures summarized in Fig. S4 have been carefully checked in the whole text - You can provide an example of the image analysis protocol in the Supplementary material The image analysis protocols are now illustrated in a supplementary figure (Fig. S3) - what did you do with the largest vesicles then? The large bubbles were excluded from the D calculations (because a proper diameter cannot be estimated) but included in the V and Nv calculations. Now specified in the revised text - can you provide a picture of the interaction charges Two pictures of interaction charges are already given in the main part of the ms, one for olivine (Fig. 7) and one for plagioclase (Fig. 4) - add reference for San Carlos olivines A reference has been added - I am confused here: are olivine and plag present in each of the interaction charges? and are they also both present at the end of each interaction experiment? Is plag never a stable phase? When there is no data reported for plag or olivine reaction rims in Table 2 does it mean that they have not been measured or that they did not occur? The section has been revised to clarify the issues raised by this reviewer and also Table 2 has been modified to improve clarity - Please indicate HP and LP in plots a and b of figure 2 Fig 2 has been corrected - can you calculate the exponential and power laws and report them into Fig 9? The power law exponents (bubble volumes between 104 to 108 μm3) are now reported in Table 3 and the paragraph about Fig 9 has been rewritten - I don't understand how you do this calculation, I obtain different values using the measured vesicle size and a time of 1000 s add this information in the methods The calculation methods for G and J are exactly those of Mangan and Cashman (1993) and Cashman and Mangan (1994) and full calculation details are given in these papers - These are bubble number densities, not nucleation rates, how do you calculate nucleation rates, add this information in the methods See answer to the previous comment - just a suggestion: can you provide a volume rendering for your samples instead of 3D views? Volume renderings are shown for 2019 samples in additional supplementary figures (Fig. S5, S6) - how about R7-2? P is 194 MPa and I can see cpx and olivine reported in Table 2 Corrected in the revised text - of what phases? Ol and Cpx. Corrected in the revised text - can you specify these different conditions All details are given in the Pichavant et al. (2013) reference - Can you cite N Le Gall paper on crystallisation of basaltic melts in EPSL 2021 here, where suppression of crystal phases due to cooling and undercooling is discussed? Difficult because that paper discusses crystallization at variable T and constant P (1 atm) whereas the section is concerned with decompression-related crystallization (variable P and nearly constant T) - not clear, please can you add picture in Supplementary material A SEM view of PST 2019-8 has been added as a supplementary figure (Fig. S7)

	- why? This section has been revised and detailed - add what you did in Methods This section has been revised and the calculations checked (see also reviewer 1) 2. My main suggestion to the authors is to take a step forward in the discussion and try and provide an integrated view of the two models underpinning paroxysm initiation on Stromboli, towards a holistic understanding of this type of activity at this volcano. Is it possible to reconcile petrological data attributing an important role to the deep-feeding system (including the authors dataset) in the initiation of Stromboli paroxysms with geophysical and petrological data (such as those from Viccaro et al. 2021, Scientific Reports) supporting instead a clear role of the shallower system? And if not, what does future petrological research need to address to fill the gap and help interpret geophysical and geochemical data better and vice versa? Again, this is not a review paper on paroxysm eruption mechanisms at Stromboli. However, a more detailed presentation of the main models is now made in the section “Implications for paroxysm eruption triggering” which is basically new. The implications of our results for the models are also more extensively discussed and progress toward a unifying phenomenological model is better emphasized
Author Comments:	Dear Editors of the "open-vent volcanoes" issue, please find here our revised contribution. The main changes from the first version are the following. (1) several new figures have been added in the Supplementary Material to follow the reviewers suggestions. (2) the final sections about paroxysm initiation mechanisms and implications for monitoring have been rewritten again to conform with the reviewers comments. For the less important changes, please see our detailed respond to editor and reviewers. Sincerely. Michel Pichavant

Timescales and mechanisms of paroxysm initiation at Stromboli volcano, Aeolian islands, Italy

Michel Pichavant[1], Ida Di Carlo[1], Massimo Pompilio[2], Nolwenn Le Gall[3, 4]

[1]Institut des Sciences de la Terre d'Orléans (ISTO), UMR 7327 UO/CNRS/BRGM
1A rue de la Férollerie, 45071 Orléans, France

[2]Istituto Nazionale di Geofisica e Vulcanologia (INGV), Sezione di Pisa
Via Cesare Battisti, 53 – 56125 Pisa, Italy

[3]Department of Mechanical Engineering, University College London
WC1E 7JE London, UK

[4]Research Complex at Harwell, Rutherford Appleton Laboratory
OX11 0FA Harwell, UK

Abstract

New textural and petrological data are presented on products from 5 Stromboli paroxysms including the two from 2019 and three historical eruptions. The data are used to constrain timescales associated with the initiation of paroxysms and to examine current models for their triggering. Samples were collected from the deposits and a subset selected for mineral separation and petrological and textural characterization. Minerals and glasses were imaged by scanning electron microscopy (SEM) and both chemical compositions and zonations were analysed by electron microprobe. Trace elements in olivine were also determined. Vesicle number densities (N_v), vesicularities (V) and vesicle sizes (D) were measured by X-ray microCT techniques. The data were systematically compared with results of experiments simulating, on the one hand, ascent, vesiculation, degassing and crystallization of LP (low-porphyricity) magmas and, on the other hand, interaction between LP and HP (high-porphyricity) magmas. Paroxysm samples are mixed and include portions representative of both LP and HP magmas. They host in variable proportions minerals and glasses texturally and compositionally typical of these two magma types. Small but systematic variations in matrix glass compositions are found between eruptions. All samples host a population of vesicles ranging from < 15 to > 1000 µm in D and whose size distributions follow mixed exponential to power law

distributions. Vesicularities are high (75% on average) and vesicle number densities range from 10^2-10^3 to 10^3-10^4 mm^{-3}. Using experimental calibrations, the textural data suggest average LP magma ascent rates of 1-2 m/s (i.e., ~1.5 hour from 7 to 1.5 km depth), much higher than most geophysical estimates. The correlation between ascent rate and textures demonstrates systematic variations between eruptions, the most energetic (1930) being associated with the highest ascent rate (~2 m/s). Widths of plagioclase reaction zones indicate that LP and HP magmas interacted for a maximum a few hours before eruption. Olivine reaction also implies durations of a few hours for LP-HP interaction and is followed by crystallization for 20 hours in the HP magma. Our results stress the fast ascent of LP magmas from their storage region and their short residence times at shallow levels before being erupted. They clarify the respective roles of the deep and shallow feeding system in the initiation of paroxysms at Stromboli. The magma blob model offers the most promising perspectives toward an integrated model of paroxysm initiation at Stromboli.

Keywords: Stromboli, paroxysms, mineral reactions, vesicle textures, experimental simulations, magmatic timescales

Introduction

The two successive paroxysms that occurred during summer 2019 (July 3 and August 28) at Stromboli (Aeolian islands, Italy) have drawn attention to this type of manifestation, the most hazardous on this volcano. These events have provided a wealth of information on geophysical signals, eruptive sequences, volumes, dispersal and nature of erupted products, all currently actively investigated (e.g., Andronico et al., 2020; 2021; Giordano and De Astis, 2020; Metrich et al., 2021; Viccaro et al., 2021). They have also stimulated a critical examination of current models for the triggering of paroxysms. In general, little is known about the origin of these highly energetic explosions which, with almost no warning, occasionally hit Stromboli and other basaltic volcanoes (e.g., Houghton and Gonnermann, 2008; Allard, 2010; Bertagnini et al., 2011; Rosi et al., 2013; Bevilacqua et al., 2020). Physical models have been developed for Strombolian-type activity (e.g., Vergniolle and Brandeis, 1996; Vergniolle et al., 1996; Parfitt, 2004; James et al., 2008; Vergniolle and Gaudemer, 2015) but counterparts for paroxysmal explosions are currently lacking. Phenomenological models are however available although they remain a matter of debate. Most petrological models have emphasized the role of the deep plumbing system. Ascent of volatile-rich LP (low-porphyricity) magma batches from their storage region (Metrich et al., 2010; 2021), together with sudden rise of deep CO_2-rich gas blobs (Aiuppa et al., 2009; 2010; Allard, 2010), would constitute the main driving forces for the initiation of paroxysms. In contrast, geophysical/volcanological models have stressed control by the volcano's shallow feeding system and dynamics. Effusive magma

eruption would induce gradual decompression of the plumbing system, drawing deep volatile-rich magma into the conduit and promoting conditions prone to the triggering of paroxysms (Calvari et al., 2011). These two models are conceptually contrasted and they lead to different monitoring strategies at Stromboli. We note that timescales of key processes such as ascent of deep volatile-rich magmas markedly contrast between the two models, ascent velocities (u) being much higher in petrological (u from 0.25 to 1.5 m/s, Pichavant et al., 2013, up to 32 m/s, Misiti et al., 2009) than in geophysical/volcanological (u = 0.003 m/s, Calvari et al., 2011) estimates. Therefore, establishing quantitative constraints on LP magma travel times from their storage region and/or on ascent velocities should enable the available phenomenological models to be evaluated and a more integrated scenario to be developed. This is the main goal of this paper which presents constraints on timescales of paroxysm initiation mechanisms.

This study is based on the acquisition of new data on samples from five paroxysms, including the two from 2019 and three historical eruptions (1930, undated and 16th century paroxysms). Two main types of data have been collected, textural and petrological. Interpretation of both kinds of data uses experiments previously performed to simulate, on the one hand, ascent, vesiculation, degassing and crystallization of LP magmas (Pichavant et al., 2013; Le Gall and Pichavant, 2016a; b) and, on the other hand, their interaction with HP magmas (Di Carlo et al., 2010). Results provide convergent estimates of short timescales for individual mechanisms preceding paroxysms and clarify the respective roles of the deep and shallow feeding system in the initiation of paroxysms at Stromboli.

Eruptions and samples studied

Eruptions investigated in this study include the two 2019 paroxysms (e.g., Giordano and De Astis, 2020; Andronico et al., 2021) and three additional historical eruptions (1930, undated and 16th century). During the summer 2019, two paroxysms occurred in less than two months, twelve years after the last similar event in 2007 (Bevilacqua et al. 2020). The first paroxysm occurred on the afternoon of July 3rd and produced an eruptive column attaining 8.4 km elevation, two pyroclastic flows which entered the sea and a small tsunami. The eruption also produced a large fall of ballistic blocks and an almost continuous spatter deposits on the volcano summit extending down to 500 m. a.s.l. on the eastern flank (our observations), much lower than reported by Giordano and De Astis (2020). Scattered ballistic bombs also reached down to 100 m elevation on the eastern lower flanks in the Timpone del Fuoco area. A plume fallout deposit covered most of the eastern flank totally blanketing the Ginostra village. Total mass of erupted material during this event has not yet been estimated, and the value of 1.4 x 10^8 kg refers only to the continuous spatter cover mapped by Giordano and De Astis (2020) while Andronico et al. (2021) provided a value of 6 x 10^7 considering

only the fallout components of the deposit. These figures should be considered as a minimal estimate since the pyroclastic flow deposits have not been included.

The second paroxysm occurred in the morning of August 28th producing an eruptive column reaching c.a. 6.4 km a.s.l. and two pyroclastic flows within the Sciara del Fuoco that spread onto the sea surface for hundreds of meters (Giordano and De Astis, 2020; Andronico et al., 2021). Also, ballistic block and spatter were observed landing as low as 400 m. a.s.l in the NE sector of the island. A fallout of lapilli and ash affected the N-NE portion of the volcano as far as the Stromboli village.

Additional eruptions studied include the 1930 and the 16th century paroxysms that are worth being compared with recent ones such as 2003, 2007 and 2019 for which several monitoring information and field data are available (Pistolesi et al. 2008, 2011; Giudicepietro et al, 2020; Ripepe et al., 2021). The 1930 and the 16th century eruptions are the largest paroxysms of the last 12 centuries (Bertagnini et al., 2011), producing a continuous blanket of spatter with a minimum volume of about 10^6 m^3 ($\approx 10^9$ kg), covering both flanks of the volcano down to 150 m. a.s.l.

Eruptive dynamics differed between the 1930 and 16th century eruptions (Bertagnini et al., 2011), making their products reference samples for paroxysm initiation mechanisms. In particular the 1930 eruption has been related to the rise of a LP magma batch strictly coupled with its own volatiles and behaving as a closed system for most of its ascent. In fact, textures of the juvenile clasts indicate that they formed by brittle fragmentation of overpressured foam after a highly vesicular LP magma batch rose through and mingled with the HP magma, immediately before its explosive fragmentation (Bertagnini et al., 2011). Conversely, for the 16th century paroxysm, a slower-rising LP magma batch was predated by a rapid ascent of a large volume of volatiles. This powerful gas outflow could have interacted with HP magmas residing in the shallow part of the feeding system, fragmenting it through "inertial fragmentation" and producing fluidal fragments of HP magmas, with only minor LP fragments (Bertagnini et al., 2011). The third eruption investigated is from an undated paroxysm older than 1930 but younger than the 16th century eruption and with a size comparable with that of 2019 paroxysms. Products from this still undated eruption define a geochemically and mineralogically primitive end-member among LP magmas (Pichavant et al., 2011), worth the comparison with less primitive products from other paroxysms. For these three eruptions, the field relations and compositions have been previously described (Bertagnini et al., 2011; Pichavant et al., 2011; Pompilio et al. 2011; Di Roberto et al., 2014).

Sampling of the 3rd July paroxysm was carried out 1 month after the event on the low eastern sector of the island village and in the Timpone del Fuoco area up to an elevation of 300 m a.s.l (Fig. 1). At Ginostra village we collected black scoriaceous and golden pumiceous lapilli accumulated on house roofs and on decks of boats brought ashore on the harbor. Along the path from Timpone del Fuoco to the summit crater we also sampled large spatter bombs (max size 50 cm) landed on the ground showing black scoriaceous, golden pumiceous and intermingled portions.

Samples of the August 28th paroxysm were collected a little more than a month after the event on the NE flank along the tourist path to the summit at an elevation between 300 and 400 m a.s.l (Fig. 1). They consist of light pumiceous and dark scoriaeous lapilli and bombs deposited on the ground between the burned vegetation and are easily recognizable from older volcanic material.

Samples of 1930 and 16th century paroxysms were collected on a natural exposure at an elevation of about 300 m. a.s.l. along the old tourist path running on the northern edge of the Sciara del Fuoco (Fig. 1), close to the stratigraphic section STR73 described in Bertagnini et al. (2011). They consist of two superimposed spatter bombs (20-40 cm thick), with fluidal appearance separated by c.a. 10 cm of epiclastic material. Both are nearly aphyric with a pumiceous and microvesicular olive-green crust often showing a bread-crust. Additionally, two samples from Bertagnini et al. (2011) were studied. PST-9 comes from an exploration trench dug along the tourist track (at about 840 m a.s.l., Fig. 1) as detailed in Pichavant et al. (2011). All investigated samples are listed in Table S1.

Methods

Sample preparation

For the acquisition of textural and petrological data, both rock fragments and mineral separates were used. Samples were gently broken into small (a few cm in size) fragments. Some were used directly for textural analysis whereas others were prepared for petrological characterization by first embedding them in epoxy resin. The mounts (25 mm diameter) were then polished and finally carbon coated.

Mineral separates were obtained by first gently crushing the samples and sieving to < 2 mm. Plagioclase and olivine plus clinopyroxene were separated by density. The concentrates were subdivided in different grain size fractions (e.g., from 0.25 to 0.5 and 0.5-1 mm). Crystals were hand-picked, embedded in epoxy resin and the mounts (containing from ~20 to 250 crystals) were polished before being carbon coated.

Petrological data

Samples were examined by scanning electron microscopy (SEM) with a Zeiss Merlin Compact microscope (ISTO, Orléans) operated at 15 kV acceleration voltage and equipped with an EDS (30 mm^2) from Bruker. Panoramas of sample fragments were made (using the Smarth Stich software from Zeiss) to identify LP and HP magma components in the sample and estimate their proportions. These panoramas also served to locate the crystals on the surface since LP magma products (i.e., golden pumices, HP magma products being designated as scoriae) are generally crystal-poor and strongly vesicular. Panoramas were made by assembling together multiple small magnification electron backscattered images. They were complemented by higher magnification

images of selected zones to characterize matrix and mineral textures and confirm mineral identification. Mineral separate mounts were examined crystal by crystal to define the textural types (Table 1), evaluate their proportions and prepare for electron microprobe analysis.

Both glasses and crystals were analysed by electron microprobe. Spot analyses were obtained using a Cameca SX Five (CNRS-BRGM laboratory, Orléans) operated under 15 kV acceleration voltage, 10 nA sample current and 10 s on peak. To avoid alkali loss, Na and K were analysed first and a defocused beam (10 µm) was used for glasses. Compositional profiles and elemental X-ray distribution maps were also obtained on selected crystals and matrices, to confirm identification of LP and HP magma components and image chemical zonations. Analytical conditions for profiles were the same as for punctual analysis and a step size of either 5 or 10 µm was used. X-ray maps of clinopyroxene, plagioclase and glass were acquired with 15 kV, 50 or 100 nA, 5-10 µm step size and dwell time 80 ms. For olivine, we used 20 kV, 400 nA, step size 5 µm and dwell time 150 ms.

Olivines were also analysed separately to determine their trace element (P, V, Co, Ni, Zn) in addition to major oxide concentrations. Specific conditions were imposed: 20 kV acceleration voltage, 80 nA sample current, counting time between 30 and 120 s depending on the element.

Vesicle textures

Vesicle textures were characterized by X-ray computed microtomography (X-ray µCT). The PST2019-4 and PST2019-8 samples were first examined using a Nikon XTH 225 micro-CT scanner at University College London (UCL, UK), operating at a voltage of 80 kV and a current of 88 µA, with 4 µm pixel size (resolution). The remaining samples were analysed at the Research Complex at Harwell (RCaH, UK) using a Phoenix V|tome|x GE s240 instrument with a voltage of 100–120 kV and a current of 100–140 µA, resulting in a spatial resolution of 3–5.5 µm. The two-dimensional (2D) projection images continuously acquired during the 360° rotation of the sample were then reconstructed using either the CT Pro 3D (Nikon Metrology, Tring) or the GE phoenix datos reconstruction software, depending on the instrument used, and processed with ImageJ (Abramoff et al., 2004, Fiji Version 1.0) and Avizo (ThermoFisher Scientific, Version 9.4).

ImageJ was first used to adjust the brightness and contrast of the images, select a Volume Of Interest (VOI) representative of the sample complexity and heterogeneity and reduce the image size to 8 bits for subsequent analysis using Avizo. Filters were then applied to the images to reduce noise and eliminate artifacts using a combination of non-local means and median filters and/or to enhance vesicle edges by unsharp masking. Segmentation of the vesicles in the VOI was then performed by interactive thresholding. Following this step, some of the vesicle boundaries were not well defined and, as a result, some vesicles appeared to be touching others excessively. To separate them, we applied two different procedures (see Supplementary Material for illustration). The first one, which was developed for the PST2019-4 sample, consisted of eroding and dilating the images prior to automatically separating the vesicles using the separate objects module. In order to optimize the

separation, the resulting images were morphologically eroded one last time. The second procedure, applied to all other samples, consisted of three morphological opening operations of the images, combining an erosion followed by a dilation, with a circular structuring element of radius 8, 4 and 1 pixel, respectively. This was then followed by further separation of the vesicles, using the separate objects module. To provide improvements to these automated vesicle separation procedures, manual correction was also performed.

After being separated, the individual vesicles were counted and analysed, using the label analysis module. Vesicle sizes (expressed as diameter D) were determined from the measured vesicle volumes, assuming a spherical shape. This assumption was found to be valid in most cases, except for the largest vesicles (a proper diameter could not be determined) and all the vesicles touching the border of the VOI which were removed from our D calculations using the border kill module. The vesicle number density (N_v) was calculated as the number of vesicles per unit volume of melt following Proussevitch et al. (2007). The vesicularity (V) of the pumice samples was obtained by dividing the measured vesicle volumes by the combined volumes of melt, vesicles and crystals. The N_v and V calculations were performed on vesicles larger than 12 μm in radius (~3 times the pixel size), the largest vesicles being included.

Experimental data

Experimental simulations were used to interpret the textural and petrological observations. The approach followed is thus analogical although, instead of analogue experiments, high temperature and pressure experiments on natural LP magmas were used and so the results are considered directly applicable to Stromboli. The experiments are of two types, decompression and interaction. The former, designed to simulate ascent, vesiculation, degassing and crystallization of LP magmas, have already been published (Pichavant et al., 2013; Le Gall and Pichavant, 2016a; b) whereas the latter, so far only presented in abstracts (Di Carlo et al., 2010), are described below. Both types of experiments started from a golden pumice from the undated paroxysm (PST-9, Pichavant et al., 2011). A homogeneous glass was first obtained by crushing the pumice and melting the powder at 1400 °C, 0.1 MPa. Then, LP-type melts were synthesized by dissolving different amounts of volatiles (series 1: only H_2O-bearing, series 2: H_2O- and CO_2-bearing, series 3: H_2O-poor and CO_2-bearing) in the glass at 1150-1200 °C and 200-250 MPa. The amounts of added volatiles were adjusted so that, for series 2, concentrations in synthesized LP melts (see Pichavant et al., 2013; Le Gall and Pichavant, 2016a; b for details) match the glass inclusion data in golden pumices (Metrich et al., 2010).

The decompression experiments started from the synthesized volatile-bearing LP-type glasses. Conceptually, they are based on the two-level structure of the Stromboli plumbing system (e.g., Pichavant et al., 2009; Metrich et al., 2010; 2021) with the LP magma storage region sitting at 7-10 km depth b.s.l. (corresponding to a P_{in} = 200-250 MPa) and the HP magma (black scoria) residing at shallower levels (P_{fin} = 50 or 25 MPa). Ascent of LP magmas was simulated from experiments where

pressure is continuously decreased from P_{in} down to P_{fin}. In most cases, a constant decompression/ ascent rate ($u = \Delta P/\Delta t$ or $\Delta h/\Delta t$ assuming a constant density of 2650 kg/m^3) was imposed (but see Pichavant et al., 2013 for experiments with variable u). In total, u ranged from 0.25 to 3 m/s and systematic data were obtained for u = 1.5 and 3 m/s (Le Gall and Pichavant, 2016a; b). Most experiments were performed isothermally at temperatures between 1140 to 1200°C (Pichavant et al., 2013; Le Gall and Pichavant, 2016a; b) thus encompassing the range for LP magmas (1150°C, Di Carlo et al., 2006; Pichavant et al., 2009). In rare cases, temperature was decreased linearly along the decompression ramp (Pichavant et al., 2013). Analytical work concentrated on bubble textures and details of the analytical procedure can be found in Le Gall and Pichavant (2016a).

The interaction experiments were designed to simulate interaction between the shallow crystal-rich HP and the deep crystal-poor LP magma during paroxysm incubation. They started from the same type of H_2O- and CO_2-bearing LP-type glasses as the decompression experiments. However, the interaction charges were seeded with mineral phases (plagioclase and olivine) representative of the HP magma. Plagioclases were 100-500 μm gem quality single crystals of composition (An 66-68) within the range of plagioclase overgrowths in the HP magma (Landi et al., 2004; 2006; 2009; Supplementary Material). For olivine, ~500 μm Fo 70-72 crystals manually separated from recent scoriae (Landi et al., 2006; 2009) were used, and also Fo 90 crystals from San Carlos (Jarosewich et al., 1980) for reference. Plagioclase and olivine were loaded with the volatile-bearing LP glass in separate $Au_{80}Pd_{20}$ capsules. For olivine, either the Stromboli and San Carlos crystals were loaded together with glass in the same capsule or capsules with only the Stromboli crystal plus glass were prepared (R9 and R10 experiments, Table 2). Experiments were all performed at 1150 °C for different durations in an internally heated pressure vessel fitted with a rapid-quench device and allowing redox control at ~NNO+1 (where NNO is the logfO_2 of the Ni-NiO oxygen buffer at P and T, Di Carlo et al., 2006). Three were isobaric (2 at ~25 MPa and 1 at ~200 MPa) and four polybaric (i.e., decompression) from P_{in} ~200 MPa to P_{fin} either ~50 or ~25 MPa, u being either ~0.64 or ~1.0 m/s (Table 2). At the end of the experiment, the glass chips hosting the mineral seeds (since plagioclase and olivine always remained present) were recovered. Reaction textures of plagioclase and olivine were investigated by SEM and the corresponding zones analysed by electron microprobe.

Results

Magma components

SEM imaging (in particular panoramas) reveals the presence of two types of components, one highly vesicular, with no or only a few crystals present and darker in BSE mode and the other bubble-poor, crystal-rich and brighter. These are found in all samples although in proportions highly variable both between eruptions and samples from the same eruption. Approximately equal proportions of each

magma component are present in some July and August 2019 samples (Table 1; Fig. S1) whereas, in others (e.g., August 2019, undated, 16th century), the denser brighter component is rare, being limited to narrow zones (50-100 µm) attached to crystals. Glasses in the two types of components have markedly contrasted compositions. The darker has low K_2O, TiO_2, P_2O_5 (not shown) and high CaO/Al_2O_3 and Mg# whereas the brighter has high K_2O, TiO_2, P_2O_5 (not shown) and low CaO/Al_2O_3 and Mg# (Table S2, Fig. 2). These chemical characteristics are typical of respectively LP (Metrich et al., 2010; d'Oriano et al., 2011; Pichavant et al., 2011; Metrich et al., 2021) and HP (Landi et al., 2004; 2006; 2009) glasses. Compared to previous studies (e.g., Metrich et al., 2010), our LP glass compositions cover a larger CaO/Al_2O_3 range and systematic variations are observed between eruptions. In the four samples analyzed from the July and August 2019 paroxysms, LP glasses have intermediate and overlapping CaO/Al_2O_3 (~ 0.64). In comparison, glasses from PST-9 are less evolved (CaO/Al_2O_3 ~ 0.68) and those from the 1930 and 16th century more evolved (CaO/Al_2O_3 ~ 0.62 and 0.55, respectively, Fig. 2). The HP are more tightly grouped than the LP glasses. In PST-9 and the 16th century samples which contain small proportions of the HP component (Table 1), HP glasses are restricted to glasses adhering to crystals and to glasses within sieve-textured plagioclase cores (16th century), the latter having the lowest CaO/Al_2O_3 in our dataset (Fig. 2).

Element X-ray distribution maps underline the strong compositional contrast between the two types of components. In zones of mutual contact, the chemical transition from one glass to the other appears sharp at the mm scale (Fig. S2). However, the transition is texturally and chemically more complex at smaller scales (< 50 µm, Pioli et al., 2014 see also Andronico et al., 2021). K_2O concentrations intermediate between LP and HP occur in glasses from the 16th century (Fig. 2a). These compositions are interpreted as partially re-equilibrated since, in the other plots (TiO_2, P_2O_5, Mg#), the two glass groups remain well separated (Fig. 2b; c).

Mineral phases

Results of SEM examination of mineral separates are compiled in Table 1, representative major and trace element compositions are given in Tables S3-S5 and a summary of the main compositional parameters of studied samples is given in Table S6. Interpretations are based on an update of the mineralogical characteristics of LP magmas presented in the Supplementary Material. In the studied samples, the major phenocryst phases are olivine, clinopyroxene and plagioclase. Apatite and Ti-bearing magnetite occur as inclusions in clinopyroxene. Apart from exceptionally rare clinopyroxene spherulites (< 10 µm, see Pichavant et al., 2011), LP matrices are microlite-free (Metrich et al., 2001; Bertagnini et al., 2003; d'Oriano et al., 2011; Metrich et al., 2010; Pichavant et al., 2011; Andronico et al., 2021). They sporadically contain small (10-50 µm) skeletal plagioclase needles representing teared off rims of plagioclase reaction zones (e.g., Pichavant et al., 2011). Below, we focus on two specific mineralogical features of LP magmas (plagioclase and olivine reactions)

because they carry information on timescales of interaction between LP and HP magmas during paroxysm incubation.

Plagioclase reaction

Plagioclase phenocrysts display abrupt compositional and textural changes (Supplementary Material, Fig. 3), the most distinctive being the development of sieve-textured zones that punctuate crystal growth and are markers of mixing and interaction between HP and LP magmas (Landi et al., 2004; see also Andronico et al., 2021). Arrival of a calcic (and also hot and volatile-rich) LP melt generates conditions promoting dissolution of plagioclase less calcic than the equilibrium composition and crystallization of a more calcic plagioclase (Tsuchiyama, 1985; Nakamura and Shimakita, 1998; Landi et al., 2004). We have simulated this reaction (Table 2). Results closely reproduce the natural plagioclase reaction texture and associated compositions (Fig. 4). Dissolution of An 68 is accompanied by crystallization of a new An 84-85 plagioclase. At the rim of the reacting crystal, a sieve-textured zone develops whose thickness (d_{plag}) progressively increases with experimental duration (Table 2). Below, we use this variation of d_{plag} with time to constrain timescales of the plagioclase reaction.

Olivine textures and reaction

Olivines in paroxysm eruption products show a wide range of textural types and compositions (Supplementary Material). Here, we focus on type 5 olivines (i.e., originated in the HP magma) and on their progressive transformation to type 4 crystals as a result of interaction with the LP magma. These olivines have cores with fine oscillatory P concentrations interpreted to reflect crystal growth (Fig. 5). Commonly, the P zonation is interrupted by a reaction zone outlined by numerous zonally disposed glass inclusions and low P concentrations. The fine oscillatory P zonation in the most external part of the crystal (Fig. 5) indicates that the reaction zone was later healed and the crystal overgrown. Therefore, two successive crystallization steps separated by a reaction episode can be identified (Fig. 5). The recognition of growth zonation in type 5 crystals enables use of olivine growth rate data to constrain timescales of crystallization in the HP magma.

Mechanisms of the reaction in type 5 olivines have been clarified from natural crystals and experimental simulations. Eruption products contain type 5 olivines showing various extents of transformation. Incipient stages start with a narrow Fo-rich (80-85) rim developed continuously around the crystal whereas the core remains unaffected. In some crystals, small reaction patches can appear but only locally at the crystal rim (Fig. 6a). When the transformation is more advanced, the reaction zone forms a continuous layer, several tens μm thick, where small melt inclusions are observed (Fig. 6b). In more advanced stages, the reaction zone with its network of melt inclusions extends to most of the crystal and the core is the only unreacted part left (Fig. 6c). The end product is a

chemically heterogeneous crystal, reversely and patchily zoned with a Fo-rich (79-84) rim zone and a Fo-poor (67-77, Table S6) core, having all attributes of a type 4 olivine.

We have simulated experimentally this reaction. In the isobaric interaction experiments (Table 2), transformations are limited to the mantling of the starting olivine by a continuous narrow (e.g., 5-10 μm in R6-1) Fo-rich (e.g., up to 86 in R6-1) rim which grades diffusively (in $\leq$ 20 μm) to the Fo 70-72 core. The texture is similar to the early reaction stages observed in natural crystals (Fig. 6a). In the polybaric interaction experiments, the reaction is extensive and 100-300 μm thick zones, texturally identical to highly transformed natural crystals develop, sharply crosscutting the P growth zonation (Fig. 6c; 7; Table 2). These reaction zones are complex. For example, in the R2-7 charge (Table 2; Fig. 7), a wide range of olivine compositions are present, from Fo 88 euhedral crystals in contact with the LP glass (Fo 86-90 in the other polybaric charges), progressively less Fo-rich domains at increasing distance from the interface to Fo 71 in the unreacted core. The zonation is typically patchy and the reaction zone is characterized by the presence of numerous melt inclusions (Fig. 6c; 7). These inclusions, distributed along crystallographic directions of the reacting olivine, are chemically specific. They have very high FeO_t concentrations (up to 18 wt% FeO_t, n.b., ~8-9 wt% in the starting LP melt, see also Bertagnini et al., 2003) and frequently contain daughter magnetite crystals (also present in naturally reacted crystals) suggesting saturation of the local melt in FeO_t. Glasses around the reacting olivines are chemically zoned. As the interface is approached, MgO decreases and Al_2O_3, SiO_2 and CaO all increase to different extents whereas FeO_t stays unchanged. MgO has the longest diffusion distances from the interface ($\geq$ 50 μm in R2-7, Table 2) and the strongest concentration gradients (i.e., 4-5 wt% MgO near the interface vs. ~8-8.5 wt% in the far-field melt in R2-7). These trends are qualitatively consistent with interface melt compositions being controlled by the combination of (1) overgrowth of Fo-rich olivine on the reacting crystal (the dark external rims observed in both the natural and experimentally reacted crystals, Fig. 6b; c; 7a) and (2) release of FeO_t from the reacting crystal to the melt. Overall, the reaction is viewed as an Fe-Mg exchange between olivine and melt, the inward flux of MgO from the melt toward the crystal (responsible for the reacting olivine becoming globally more Fo-rich) being counteracted by an outward flux of FeO_t. Implications for the kinetics of the olivine reaction are discussed below.

Vesicle textures

The textural data are reported in Table 3 and representative textures illustrated in Fig. 8, S5 and S6. Although being all quite similar, some samples stand out of the main group. PST 12LP (16^{th} century eruption) is texturally composite with a scoria-like and another more typically pumiceous part, each subjected to a separate X-ray μCT analysis (Table 3). PST 2019-8 (August 2019 eruption), texturally specific according to SEM observations (Fig. S7), has textural parameters systematically outside the other samples, as detailed below. Nevertheless, all samples (including the scoria-like part of PST 12LP) host a population of vesicles, spherical for the smallest to more ellipsoidal for the

largest, with similar D_{av} (36-94 µm if the scoria-like PST 12 LP sample is included, 36-76 µm if not, Table 3). This vesicle population covers quite a large range of sizes, from 12-15 µm for the smallest to 393-1141 µm for the largest (Table 3). All samples have the same minimum D (D_{min}, 12-15 µm) but complementary SEM observations indicate that vesicles < 12 µm (i.e., smaller than 3 x resolution) are also present (Fig. S7). In contrast, maximum D values (D_{max}) vary from one sample to the other, the highest being found in PST 2019-8 where large, irregularly shaped and interconnected vesicles are present (Fig. S7). Counterintuitively, this last sample is also the one with the lowest D_{av} (Table 3) although D_{av} is underestimated because the largest irregular vesicles were not counted (technical and shape constraints prevent D to be calculated). V ranges from 49 to 86% (71% on average) if the data for the scoria-like PST 12 LP are included and from 69 to 86% (75% on average) if not (Table 3). Again, PST 2019-8 is the sample with the highest V. Vesicle number densities (N_v) cover a range > 1 order of magnitude, from 10^2-10^3 mm^{-3} (e.g., 720 mm^{-3} in the more scoria-like part of PST 12LP) to 10^3-10^4 mm^{-3} (e.g., 8075 mm^{-3} in PST 217, 1930 eruption), the maximum N_v (8196 mm^{-3}) being found in PST 2019-8 (Table 3). N_v negatively correlates with D_{av}, and also with D_{max} except in PST 2019-8 and, so, samples with the highest N_v (1930 eruption) have the smallest vesicles. Vesicle size distributions (VSD) mostly follow mixed exponential to power law behaviour, as observed for the April 5 2003 and March 15 2007 paroxysms (Polacci et al., 2009) and for experimental H_2O- and CO_2-bearing melts (series 2, Le Gall and Pichavant, 2016a; b) decompressed to 50 and 25 MPa (Fig. 9). The small- to medium-sized vesicles can be fit by exponential functions and, so, this population reflects a mechanism of near-equilibrium nucleation and growth (Polacci et al., 2009; Le Gall and Pichavant, 2016a; b). Power law regressions fit the medium- to large-sized vesicles, interpreted as indicating far-from equilibrium degassing corresponding either to coalescence events or to continuous nucleation of new vesicles (Polacci et al., 2009; Le Gall and Pichavant, 2016a; b). The distribution for PST 2019-8 is clearly different, being closer to power law than to exponential (Fig. 9) and the power law exponent is lower than for the other samples (Table 3). If the natural VSD distributions are fitted with the method of Mangan et al. (1993) and Cashman and Mangan (1994), bubble growth rates (G) from $9x10^{-3}$ to $3.5x10^{-2}$ µm/s are obtained (calculations performed assuming a vesiculation time of 1000 s for all samples), 1-2 orders of magnitude slower than when calculated from parabolic growth models (Sparks, 1978; Navon and Lyakhovsky, 1998). Nucleation rates (J), negatively correlated with growth rates, range from 0.56 to $2.31x10^{-7}$ events / $µm^3$. s, PST 217 (1930 eruption) being the sample with the maximum J.

Our N_v and V data are both higher and the D_{av} data lower than in 2003 and 2007 samples (Polacci et al., 2006; 2009; Table 3). The scoria-like part of PST 12LP (16^{th} century eruption) is the only sample in our dataset with N_v (720 mm^{-3}) in the range of the 2003 and 2007 samples (643 and 860 mm^{-3} respectively, Table 3). This is likely a consequence of the higher resolution in this than in previous work (3-5.5 µm vs. 9-14 µm in Polacci et al., 2009) which leads to more importance being given to the small vesicles. Yet, VSD and power law exponents are similar in both studies (Fig. 9;

Table 3). Using a 2D approach, N_v in the 10^3-10^4 mm^{-3} range and average V of 50% were found for July and August 2019 samples (Andronico et al., 2021), respectively broadly similar and lower than in this study. Vesicle diameters (8-20 µm for July, 4-16 µm for August 2019) are smaller in Andronico et al. (2021) than in this work (D_{av} of respectively 36 and 55-76 µm, Table 3), most probably the result of methodological differences between the two studies (diameters respectively determined from peaks in size histograms and from measured vesicle volumes assuming a spherical shape).

Discussion

Ascent-related crystallization

Since the recognition of the fundamentally polybaric nature of the Stromboli plumbing system, the possibility of ascent-related crystallization has received strong attention (e.g., Metrich et al., 2001). One of the motivations is that crystallization, if resulting from LP magma ascent from its storage region, would offer the potential to constrain ascent durations and velocities. In this context, the observations that, first, LP magma are crystal-poor and, second, that their matrices are microlite-free (Metrich et al., 2001; Bertagnini et al., 2003; d'Oriano et al., 2011; Metrich et al., 2010; Pichavant et al., 2011; Andronico et al., 2021; this study) are critical. They imply that crystallization does not occur during LP magma ascent. Note that it is theoretically possible that crystals form at depth in the plumbing system and dissolve when the magma reaches shallower levels (Di Carlo et al., 2006 and see below). In any case, there is a difficulty in confidently identifying decompression-related crystals in LP magma products and this seriously weakens the possibility of constraining ascent velocities from crystallization kinetics.

The near lack of ascent-related crystallization is consistent with results of decompression experiments on LP melts. These experiments have covered a range of temperatures, initial and final pressures, decompression rates and initial melt volatile concentrations, summarized above (Pichavant et al., 2013; Le Gall and Pichavant, 2016a; b). With the exception of one charge in the R16 experiment (R16-1, Table 2), crystallization was never observed. The polybaric interaction experiments reported in this study also did not crystallize (Table 2, only the isobaric experiments performed at ~200 and ~25 MPa contain a few olivines and clinopyroxenes). The absence of crystallization during decompression has been often given a kinetic interpretation (e.g., Metrich et al., 2021). Indeed, partial crystallization of olivine and clinopyroxene is observed in the R16-1 charge which comes from the longest (~8.3 h) decompression experiment performed so far. However, a second charge in the R16 experiment (R16-2, Table 2) shows no evidence for crystals being present. Although the causes of the discrepancy between the two R16 charges (ran together) are not completely clear, the important point is that R16-1 and R16-2 started from two LP glasses synthesized under dissimilar P-T conditions and containing significantly different initial H_2O and CO_2 concentrations (details in Pichavant et al., 2013).

Therefore, the crystal-bearing R16-1 charge must be considered as exceptional. Volatile-bearing LP melts crystallize very rapidly as soon as placed under their liquidus since fast quench techniques are necessary to prevent quench crystallization in the experiments (e.g., Di Carlo et al., 2006). Consequently, partial crystallization in R16-1 is unlikely to be explained by kinetic considerations. Our preferred interpretation is that one of the two R16 charges crossed its liquidus during decompression whereas the other did not (see Di Carlo et al., 2006 for discussion of decompression paths).

There is broad agreement on the average temperature of LP magmas (1150°C) and of the HP body (1100°C, e.g., Di Carlo et al., 2006; Pichavant et al., 2009). However, the temperature gradient during ascent of LP magmas is less well constrained. Di Carlo et al. (2006) showed that the slope of the P-T ascent path is the main factor controlling whether a LP melt would cross its liquidus (i.e., crystallize) during ascent or not. An adiabatic ascent will not lead to crystallization (it is even possible that the melt becomes superheated) whereas a path associated with a progressive temperature decrease from 1150 down to 1100°C will induce crystallization (Di Carlo et al., 2006). The euhedral sector zoned type (1) diopsidic clinopyroxene microphenocrysts common in our paroxysm samples (Fig. S4f) require a degree of undercooling (ΔT) of ~20-40°C to form; for either lower or higher ΔT, textural and compositional characteristics unlike natural crystals would be obtained (Masotta et al., 2020). Rims in type (4) clinopyroxenes have the same Mg# and Wo as type (1), (2) and (3) crystals (Supplementary Material, Table S6) and, so, LP melts did not significantly fractionate before intruding the HP body. Quite frequently, type (3) olivine microphenocrysts are found attached to these type (4) clinopyroxenes, crystallizing partially engulfed in diopsidic rims (Fig. S4i, see also Andronico et al., 2021) and suggesting crystallization in response to fast cooling against HP augites. Therefore, ΔT estimates, compositions and textures suggest the persistence of a thermal contrast between intruding LP magmas and the resident HP body. This implies a steep P-T slope during most of the ascent path, closer to adiabatic than to progressive cooling and consistent with the near absence of decompression-related crystals. Again, the critical factor controlling crystallization is the temperature gradient during LP magma ascent.

LP magma ascent rates

N_v and D for the natural samples are compared with their experimental counterparts (Fig. 10). The calibration data exclusively come from the decompression of LP-like H_2O- and CO_2-bearing melts (Pichavant et al., 2013; series 2 in Le Gall and Pichavant, 2016a; b). Although experimental charges are small (pluricentimetric at maximum), vesiculation takes place over length scales that are mostly 10-100 µm, rarely larger and, most importantly, similar in experiments and natural samples. Therefore, direct use of experimental results is warranted. In general, the natural N_v and D_{av} data are closely reproduced by the experiments. For a fixed final pressure (P_{fin}) along the decompression ramp (either 50 or 25 MPa, Fig. 10a), experimental N_v increase with increasing u. This is consistent with higher

decompression rates promoting a larger number of bubbles because the highest the u the highest the degree of volatile supersaturation in the melt (e.g., Toramaru, 1995; 2006). N_v in paroxysm eruption products are reproduced for u between ~2 and ~3.2 m/s (final ascent to 25 MPa) or between ~2.8 and > 3 m/s (final ascent to 50 MPa). In the same way, decreasing P_{fin} at constant u raises the degree of volatile supersaturation in the melt which increases N_v (Fig. 10b). For u = 3 m/s, N_v in natural samples are reproduced for final ascent to between ~20 and ~55 MPa whereas, for u = 1.5 m/s, the range of natural N_v is intersected only partially and at very low P_{fin} (< 10 MPa, Fig. 10b). Ranges of D_{av} in natural products (excluding the 2003 and 2007 products) are well reproduced at 25 MPa but not at 50 MPa P_{fin} whatever the ascent rate (in the 1.5-3 m/s range) thus suggesting that 50 MPa (~1.8 km b.s.l.) is a maximum for the LP magma final ascent level (Fig. 10c). Last, bubbles generated for u = 3 m/s have slightly too low D_{av} compared to natural vesicles whatever the P_{fin}. The range of natural D_{av} requires, to be reproduced, u slightly lower than 3 m/s and a P_{fin} ranging between ~15 and ~45 MPa (Fig. 10d).

These constraints require testing on two critical aspects. *First*, the calibrating experimental database is limited to P_{fin} = 25 MPa minimum. Although magma fragmentation levels are poorly known for Stromboli paroxysms, LP glasses in PST 2019-10 (August 2019) as well as in PST 2019-1 and PST-9 contain 1.09, 1.11 and 1.16 wt% dissolved H_2O (SIMS analyses, Pichavant et al., 2020). This corresponds to H_2O solubilities at 13-14 MPa which implies that LP melts ascended to P_{fin} < 25 MPa. From Fig. 10b, overestimating P_{fin} will underestimate experimental N_v (by < 0.5 order of magnitude), leading to slightly overestimate u (by < 0.5 m/s, Fig. 10a). Vesicle D_{av} will be also underestimated (Fig. 10d). *Second*, the experimental calibrations are for 1200°C which is too high a temperature for LP melts (1150°C). Correcting for temperature using a vesiculation model is presently not possible given the small number of experiments on vesiculation in basaltic melts (Shea, 2017; Nishiwaki and Toramaru, 2019). In addition, all theoretical studies of bubble vesiculation consider H_2O as the sole volatile component (e.g., Toramaru, 1995; 2006; Navon and Lyakhovsky, 1998; Shea, 2017). Therefore, the experiments of Pichavant et al. (2013) performed at 1150°C and for the same melt and volatile compositions as the 1200°C experiments will be used to constrain the effect of temperature. Charge R5, decompressed to 25 MPa at u = ~1 m/s, has N_v plotting above the 25 MPa P_{fin} 1200°C isobar (if extended to u = 1 m/s, Fig. 10a), indicating that, at constant P_{fin} and u, N_v increases from 1150 to 1200°C. Another 1150°C charge decompressed to 45 MPa P_{fin} (R1, Pichavant et al., 2013) shows the same trend. Such a dependency probably reflects the decrease of volatile diffusivities as temperature decreases thus favouring bubble nucleation rather than growth, although other explanations (dependence of surface tension with temperature) are possible. Thus, a temperature overestimation leads to a N_v underestimation and, therefore, to an overestimation of u. Correcting for temperature requires experimental N_v to be increased by ~1 order of magnitude (see the 25 MPa P_{fin} isobar in Fig. 10a) which corresponds to a reduction in u by 1 m/s (i.e., at 25 MPa P_{fin}, from ~2 to 1

m/s and from 3.2 to 2.2 m/s). We conclude that the calibrating 1200°C experimental u data need negative corrections by 1-1.5 units to be fully applicable to LP melts.

Estimates of ascent velocities for LP melts are compared in Fig. 11. A large dispersion, covering several orders of magnitude, is apparent. Most geophysical/volcanological estimates yield very low u (10^{-4}-10^{-2} m/s) and these might not actually all correspond to LP magma flow. The recent ground deformation model of Ripepe et al. (2021) calculates ascent rates much higher than all previous geophysical/volcanological estimates, between 15.3 m/s (July 3, 2019) and 9.5 m/s (August 28, 2019) for the "expanding gas-magma mixture". Concerning petrological estimates, the ascent velocity of 32 m/s (Misiti et al., 2009) is considered too high as it relies on an elevated LP melt H_2O content (3.79 wt%) which strongly impacts the viscosity and density calculations, and also on assumptions on ascent flow regime. Our own estimates converge toward ascent velocities of 1-2 m/s (Fig. 11). This range must be considered as an average given the possibility of vertical as well as lateral variations in velocity in the conduit (Massol and Jaupart, 1999). However, there is no indication in our natural vesicularity data for an accelerating velocity since VSD (Fig. 9) are well simulated by decompression experiments performed at constant u. Note that u = 1 m/s implies a duration of 92 min (~1.5 h) for LP melts to ascend from 7 to 1.5 km.

Textural variability between paroxysmal eruptions

In what precedes, paroxysm eruption products have been considered globally. Yet, systematic textural differences exist between our samples. The N_v data cover a range > 1 order of magnitude, correlated with changes in vesicle D (Table 3), and differences in VSD have been noticed (Fig. 9). If the comparison is restricted to samples with similar VSD (i.e., discussing PST 2019-8 apart), the N_v range can be attributed to variations in either u (Fig. 10a) or P_{fin} (Fig. 10b), although large differences in P_{fin} between eruptions appear unlikely given the homogeneous LP matrix glass H_2O concentration data (from 1.09 to 1.16 wt%, Pichavant et al., 2020). The H_2O/CO_2 ratio of the LP melt could have an influence (compare results in series 2 and 3 in Le Gall and Pichavant, 2016a; b) but large variations in H_2O/CO_2 are not recorded in glass inclusions representative of LP melts prior to decompression (Metrich et al., 2010). Therefore, u can be taken as the main N_v controlling variable, in agreement with theoretical models (e.g., Toramaru, 2006; Shea, 2017). In this context, the sample which records the highest N_v and, consequently, the fastest u (~2.2 m/s, Fig. 10a) is PST 217 (1930 eruption, Table 3). If the correlation between N_v and u is extended to the other samples (again excluding PST 2019-8), a progressive decrease in u from the 1930 to the 16th century eruption is observed, with the July 2019 and the undated eruption (PST-9) lying in between. Previous studies have established positive correlations between N_v and eruption energy indicators such as the column height (Toramaru, 2006) and explosivity (Polacci et al., 2006; 2009). Therefore, our results confirm that 1930 is the most energetic among the studied eruptions (Bertagnini et al., 2011). The 16th century eruption has the lowest N_v and so the slowest u. This is consistent with differences previously inferred in ascent rates

and fragmentation mechanisms between the 16th century and the 1930 eruptions (Bertagnini et al., 2011) and with the compositions of the 16th century LP glasses which are the most evolved (lowest CaO/Al_2O_3, Fig. 2). In comparison, other petrological indicators such as olivine composition do not simply correlate with eruption energy (e.g., Metrich et al., 2021) since the undated and the July 2019 eruptions have similar N_v (Table 3) but contrasted Fo max (Table S6). We conclude that N_v stands as a promising tool to scale energies of paroxysmal eruptions at Stromboli.

The negative correlations between N_v, D_{av} and D_{max} can be rationalized simply by using N_v as a proxy for u because higher u imply shorter timescales for the vesicles to grow hence lower D. Therefore, the D systematics add confirmation to the ranking made above between the different eruptions since PST 217 (1930 eruption) has the lowest D_{max}, one of the two lowest D_{av} (Table 3) and the highest J. However, the correlations break if PST 2019-8 (August 2019 eruption) is included. SEM imaging of this sample reveals large irregularly shaped vesicles. Small vesicles are found distributed in thin glass filaments surrounding the large vesicles (Fig. S7). These specific textural characteristics correlate with the marked power law behavior (Fig. 9) and the lower power law exponent (Table 3) in PST 2019-8 compared to the other samples. Vesiculation in PST 2019-8 appears to have mixed characteristics, intermediate between pumices and scoriae. Large irregularly shaped vesicles and numerous small vesicles located between the largest are typical of scoriae (Polacci et al., 2009). The marked power law behavior in this sample, which is also an attribute of scoriae (Polacci et al., 2009), would reflect coalescence combined with a late vesiculation event (since the small vesicles occur in stretched and deformed melt films, i.e., in an expanding magma, Fig. S7). The degassing evolution in PST 2019-8 proceeded to a stage more advanced than in the other samples.

LP-HP Magma interaction

Following ascent from their storage region, arrival of LP magmas at shallow levels generates mechanical, thermal and compositional perturbations in the HP magma body. Both magmas interact and plagioclase and olivine reaction textures record mechanisms and timescales associated with this interaction. Previous plagioclase dissolution experiments similar in principle to those in this study (Table 2; Fig. 4) but performed in the diopside-anorthite-albite system at 0.1 MPa (Tsuchiyama, 1985) have shown that, for conditions as in our experiments (reacting plagioclase less An-rich than the equilibrium plagioclase) and temperature being constant, d_{plag} increases proportionally to the square root of time. This observation, which suggests that diffusion in plagioclase is the limiting mechanism (Tsuchiyama, 1985), provides a theoretical framework for estimating timescales of the plagioclase reaction in Stromboli products ($d_{plag} = t^{0.5}$). The d_{plag} data in both the isobaric and polybaric experiments have been regressed as a function of time. Using the 6 data points (Table 2), a power law exponent of ~0.65 is obtained, in reasonable agreement with the dependence with $t^{0.5}$ found by Tsuchiyama (1985). Therefore, plagioclase reaction zones of ~100 µm require 5.5 h (329 min) to form. Since 100 µm is approximately the maximum reaction width observed in eruption products

(Supplementary Material, Fig. 3), 5.5 h is considered as a maximum duration for the plagioclase reaction. We note that the timescales calculated from plagioclase do not largely change with the reaction width. A duration of 15.6 h is obtained for a d_{plag} of 200 µm (gross overestimation). Last, power law regressions derived from 5 instead of 6 points have been also tested to account for the variability of the d_{plag} data for durations of ~100 mn (Table 2). For d_{plag} = 100 µm, durations of 2.3 and 13.7 h respectively are calculated by removing the point with either the lowest (R6-2) or the highest d_{plag} (R4-5, Table 2) from the regression. Thus, plagioclase reaction timescales are consistently in the range of hours (Fig. 11).

Since the P zonations in olivine (Fig. 5) have a magmatic origin, timescales of crystallization in the HP body can be estimated from the olivine growth rate (G). Using the crystal of Fig. 5 and taking G = 10^{-9} m/sec, (e.g., Shea et al., 2019), growth durations of the order of 200 h (~8 days) are obtained for the core, and 20 h for the overgrowth. It is important to stress that these values are highly dependent on the olivine growth rate chosen. The value taken above is in the lowest range for olivine (Shea et al., 2019), but consistent with the low degrees of undercooling expected in the HP magma where thermal balance is probably established globally given the chemical homogeneity of its mineral phases. Therefore, the growth durations obtained above are considered as maximum values. To overgrow the fossil reaction zone in Fig. 5, crystallization resumed for 20 h maximum before the crystal was erupted (Fig. 11).

Timescales of the olivine reaction are more difficult to quantify since the reaction is complex and involves diffusion in both olivine and melt. Although the experiments produced reaction zones of widths comparable to natural crystals, charges R6-1 (isobaric) and R5-3 (polybaric) have contrasted d_{ol} and textures, yet their durations differ relatively little (115 vs. 110 min, Table 2). Therefore, caution should be exercised with the use of experimental d_{ol} to infer reaction timescales. In R6-1, the reaction involved a degassed melt with dissolved H_2O and CO_2 concentrations controlled by their ~25 MPa (Table 2) solubilities. In contrast, in R5-3 (and in the other polybaric charges), the reaction was initiated at 200 MPa from an undegassed LP melt. As pressure dropped during the experiment (Table 2), the reacting melt became progressively degassed and volatile concentrations decreased. For the initiation of the olivine reaction in R5-3 and R6-1 melts respectively, H_2O concentrations of ~3 and ~1.5 wt% can be estimated (e.g., Pichavant et al., 2013). Given the strong influence of H_2O on melt diffusivities (e.g., Zhang and Ni, 2010), mass transfer in the melt was initially faster in the polybaric than in the isobaric experiments, thus favouring the preferential development of the reaction in R5-3 than in R6-1. If placed in the natural context where the olivine reaction is assumed to be initiated at a maximum of ~50 MPa (~1.8 km) in the HP body, R5-3 and the other polybaric experiments thus overestimate the advancement of the olivine reaction. This implies that 110 mn (or 173 mn, the duration of the longest polybaric experiment, Table 2) is a minimum for the development of natural olivine reaction textures as in Fig. 6c. By opposite, the R6-1 charge underestimates the advancement of the olivine reaction because (i) magma interaction can occur at pressures higher than 25 MPa and

(ii) intruding LP melts can be supersaturated in H_2O (Le Gall and Pichavant, 2016a). Therefore, 115 mn (Table 2) is a maximum for the development of natural olivine reaction textures as in Fig. 6a. Overall, the natural olivine reaction textures record timescales ranging from < 115 min (< ~2 h) for the early to > 173 min (> ~3 h) for the more advanced stages, globally in the range of a few h (Fig. 11).

Implications for paroxysm triggering mechanisms

Different phenomenological models are available for paroxysm initiation mechanisms. The triggering of paroxysms has been attributed to the arrival of LP crystal-poor and volatile-rich (H_2O, CO_2, S, Cl) magma batches in the shallow part of the feeding system ("magma blob model", Bertagnini et al., 2003; Metrich et al., 2010; 2021). By opposite, in the "gas blob model" of Allard (2010), the main driving force in the initiation of paroxysms is the gas phase. Large CO_2-rich gas blobs generated by foam collapse in the deep plumbing system ascend rapidly together with entrained LP melts toward the surface where they expand and burst (Allard, 2010). In contrast to these models based on the arrival of either melt or gas from the deep feeding system, others have attributed to the shallow system the main role in the initiation of paroxysms. Calvari et al. (2011) observed that the two 2003 and 2007 paroxysmal eruptions were preceded by the effusion of a similar volume of lava. Thus, the top part of the feeding system became depressurized, drawing LP magmas up to higher levels in the conduit and allowing the explosive fragmentation threshold of Namiki and Manga (2006) to be overstepped. Although the two types of models are traditionally opposed, there are also models with roles for both the deep and shallow feeding systems. The large increase in CO_2 flux prior to the 2007 paroxysm was attributed to a deep CO_2 source but the cause of the excess CO_2 degassing was assigned to shallow lava effusion and depressurization of the feeding system (Aiuppa et al., 2010). The role of the shallow feeding system is also observed to vary between eruptions. The July 2019 eruption was not preceded by long-lasting effusive activity (only a small lava flow about 45 mn before the July 3 paroxysm, Andronico et al., 2021) at the difference of the 2003 and 2007 events. However, the specific seismic and ground deformation signals (Giudicepietro et al., 2020; Ripepe et al., 2021) coupled with the Li enrichment in plagioclase crystal rims (Viccaro et al., 2021) leave little doubt that near surface processes were involved in the triggering of the 2019 paroxysms.

Results presented in this paper stress the short timescales associated with paroxysm initiation mechanisms, consistent with previous constraints based on the transition from exponential to power law behavior in pumices (from min to hours, Polacci et al., 2009). Durations of LP magma ascent from their storage region are of the order of hours (e.g., 1.5 h for u = 1 m/s, Fig. 11). These short timescales are consistent with the durations determined for the growth of type 3 olivine crystals (4-46 hours maximum, Bertagnini et al., 2003). In the same way, the shortest diffusion timescales calculated for mainly type 1 olivines (a few days, Metrich et al., 2021) can be taken as maximum durations for LP magma ascent. It is worth noting that short timescales for LP magma ascent at Stromboli are not totally unexpected. Aiuppa et al. (2010) interpreted the nearly crystal-free nature and vesicularity

textures of yellow pumices to indicate ascent within hours from the deep reservoir. The slow LP magma ascent velocity (0.003 m/s) derived from lava emission rates by Calvari et al. (2011) is relevant only for the upper part of the conduit. For deeper LP magma transport, faster velocities and shorter timescales were actually considered (hours to days, Calvari et al., 2011). In fact, the Calvari et al. (2011) model would apply more easily for ascent rates > 0.003 m/s (shorter LP column heights would be needed for the explosive fragmentation threshold to be overstepped). Last, the maximum mean speed proposed for CO_2-rich gas slugs generated by foam collapse (1.1 m/s, Allard, 2010) is almost indistinguishable from the average LP magma ascent rate proposed in this study (1-2 m/s, Fig. 11). This would favour closed-system degassing (no gas-melt separation) upon ascent which agrees with the magma blob (Metrich et al., 2021) but not with the gas blob model (Allard, 2010). Gas segregation is difficult in fast ascending basaltic magmas (Parfitt, 2004).

Our results also show that the physical interaction between LP and HP magmas before paroxysmal eruptions do not last for long durations. Timescales of plagioclase reactions in the HP magma are in the range of a few hours (Fig. 11). Such durations are sufficient for type 5 olivines from the HP magma to react to type 4 crystals. Further crystallization in the HP magma lasts for a maximum of 20 hours. However, the range of timescales for magma interaction is much longer than the durations associated with Li diffusive incorporation in plagioclase rims (maximum 180 s, Viccaro et al., 2021). This implies that the Li data record events immediately preceding the paroxysmal eruptions, probably related to explosive vesiculation and fragmentation (see below). This emphasizes the contrast with mechanisms such as LP magma ascent and LP-HP interaction whose timescales are of the order of hours.

Paroxysmal eruptions often occur as part of long periods of abnormal activity. The March 2007 paroxysm was preceded by a two weeks period of high CO_2 flux (Aiuppa et al., 2009; 2010). In the same way, prior to the July 3, 2019 event, an increase of the normal explosive activity from several days before the eruption was noted and a major explosion occurred on June 25 (Giordano and De Astis, 2020). The July-August period preceding the August 28, 2019 paroxysm was characterized by more energetic Strombolian eruptions, high heights of ejecta, frequent ash fallout and lava effusion (Giordano and De Astis, 2020; Andronico et al., 2021). Therefore, as far as timescales are concerned, any phenomenological model for paroxysm initiation at Stromboli must combine mixed timescales, i.e., durations of a few hours for individual mechanisms (LP magma ascent, LP-HP interaction) with perturbations of the shallow plumbing system lasting for weeks to months (Andronico et al., 2021). This can be achieved by observing, on the one hand, that small batches of LP magma quasi-permanently recharge the shallow part of the plumbing system (D'Oriano et al. 2011). In the same way, the H_2O/CO_2 ratios of explosion gases during normal activity require a contribution from the deep feeding system (Pichavant et al., 2009). Therefore, communication between the deep and shallow parts of the feeding system can be considered as permanent, consistent with the fast LP magma ascent rate demonstrated here and in agreement with the maintenance of a steady-state volcanic activity over

two millennia. On the other hand, the repetition of sieve-textured and overgrowth zones in plagioclases (Fig. 3; Landi et al., 2004) and the presence of reaction zones in type 5 olivine cores (Fig. 5; 6b) require either that HP crystals accidentally survived LP magma recharge or, most probably, that LP-HP magma interaction was not followed immediately by an eruption. Thus, not all LP magma recharge events lead to a paroxysmal eruption; arrival of LP magmas at shallow levels is a necessary but not a sufficient condition for a paroxysmal eruption to occur. Given the high petrological, mineralogical and geochemical homogeneity of yellow pumices (e.g., Pompilio et al., 2011), specific conditions must be established in the shallow rather than in the deep plumbing system to trigger a paroxysm.

Although none of the paroxysm initiation models mentioned above fully explain all observations (e.g., Aiuppa et al., 2010), the magma blob model, with possible feedback between the shallow and deep parts of the feeding system, is considered to offer the most promising perspectives toward an integrated phenomenological model of paroxysm initiation at Stromboli. In comparison, the gas blob model raises more problems. Besides the LP melt ascent rate issue discussed above, the model implies vesicle D in the foam increasing from 140-170 μm at 10 km to 800-1100 μm at 3 km (Allard, 2010), much larger than average vesicle sizes in yellow pumices (Table 3) and decompression experiments (Fig. 10). The model also predicts a very high gas fraction (98%) in the erupted mixture at the vent (Allard, 2010) and is seriously undermined by disequilibrium CO_2 degassing (Pichavant et al., 2013; 2019) which challenges in a fundamental way the interpretation of gas ratios and degassing paths. In the frame of the magma blob model, paroxysm initiation starts with the ascent of a LP magma batch from its storage region, following mechanisms discussed above for crystallization (or lack of) and vesiculation. It is likely that a minimum cumulative LP magma volume is necessary to account for masses and mass fluxes erupted (e.g., Metrich et al., 2021) and for the heightened activity during periods preceding paroxysms (see above). However, a volume threshold is considered unlikely given the continuity in energy and magnitude between paroxysms and major explosions and the scale-invariance observed in their respective conduit processes (Ripepe et al., 2021). Upon ascent, LP magma degassing occurs mainly under closed-system as discussed above and generates relatively small vesicle sizes < 100 μm (Table 3). We stress that there is no indication in our vesicularity data, whether natural or experimental, for the presence of large gas pockets or slugs as commonly assumed at Stromboli (e.g., Allard, 2010; Viccaro et al., 2021). While being aware that size arguments can be opposed here (e.g., gas slugs would be larger than natural or experimental samples), it is recalled that, for a given melt viscosity and surface tension, large vesicles imply small gas overpressures because the overpressure in a vesicle growing by diffusion is inversely correlated with D (e.g., Proussevitch et al., 1993). Therefore, vesicles that had grown diffusively to gas slug sizes hardly have the capacity to keep overpressures in the range required by the dynamics of paroxysmal eruptions (see below). However, the situation would be different in the case of vesicles grown by coalescence. Either

coalescence or nucleation of new bubbles are observed in the VSD of natural LP samples (Fig. 9; Polacci et al., 2009) but overall coalescence is of minor importance except in scoriae.

In fact, the remaining difficulty with the magma blob model is the generation of overpressure, to account for the highly explosive Vulcanian dynamics that ultimately characterize paroxysms (e.g., Allard, 2010; Giordano and De Astis, 2020). Previous studies have attributed to the colder, more crystallized and viscous HP magma body an essential mechanical role ("plug") in limiting ascent of the rising LP magma "piston" (e.g., Giordano and De Astis, 2020). The 3 months clogging of the conduit in 2003 was interpreted to promote the generation of overpressures (Calvari et al., 2006). However, it is unclear if sufficiently high overpressures, typical of paroxysms (up to ~8 MPa in 2007 from ballistic block ejection velocities, Pistolesi et al., 2011, see Allard, 2010 for 2003 and Andronico et al., 2021 for 2019), can be developed mechanically, either by a "plug" effect or conduit obstruction. Therefore, a mechanism of internal overpressurization of the LP magma is favoured here although we recognize that the explosive degassing and fragmentation of high temperature, crystal-poor low viscosity magmas such as the LP still requires to be fully elucidated. Viscous retardation of vesicle growth (e.g. Sparks et al., 1994) can be ruled out as an overpressurization mechanism because LP magma viscosities (Misiti et al., 2009) remain low, not exceeding 10^2-10^3 Pa s maximum. Even if provision is made for decreasing melt H_2O concentrations during ascent, presence of gas bubbles and cooling due to the HP body, LP magma viscosities are in a range where no limiting influence of viscosity on diffusive vesicle growth is expected for ascent velocities as in this study (Sparks et al., 1994). The limited degassing efficiency and low permeability of yellow pumices (up to 2 orders of magnitude lower than in scoriae) has led to the suggestion that LP magmas could become overpressurized as a result of gas accumulation at the top of the magma column (Polacci et al., 2009). Indeed, the vesicularity data (75% on average, Table 3) are in the appropriate range for fragmentation to occur, but such a mechanism of progressive gas accumulation followed by fragmentation appears more typical of Hawaiian (Parfitt, 2004) than of Vulcanian (i.e., shallow sudden release of overpressure within a small magma batch undergoing closed degassing, Giordano and De Astis, 2020) style. Pichavant et al. (2013) suggested that CO_2-oversaturated melts generated by disequilibrium degassing during decompression could explosively degas and fragment when held at shallow pressures but this hypothesis has remained untested. Yet, fragmentation was observed in some decompression experiments (Le Gall and Pichavant, 2016b) and tentatively interpreted to result from a late vesicle nucleation event (Massol and Koyaguchi, 2005). Presently, the only work that accounts for an explosive degassing behavior in low viscosity basaltic magmas is that of Namiki and Manga (2006). Disequilibrium vesicle expansion accompanied by explosive degassing, fragmentation and bubble film rupture was observed during fast decompression of bubbly fluids; vesicles expanded with an upper velocity limit determined by the enthalpy change associated with the decompression (Namiki and Manga, 2006). Although based on experiments performed with analog materials, a threshold for the explosive/effusive transition in basaltic magmas was defined. The main variables in the model are the

decompression rate, vesicularity and the height of the bubbly magma column and so the model has general potential applicability, for example to major explosions as well as to paroxysms. However, it remains to be tested experimentally on real LP magmas. Another domain where additional research is needed is the interpretation of geophysical signals. The compatibility between the seismic and deformation signals immediately preceding (< 10 min) the 2019 paroxysms (Giudicepietro et al., 2020; Ripepe et al., 2021; Vicarro et al., 2021) and the final ascent of an overpressurized LP magma batch needs to be explored. We conclude that more work is needed to fully understand the generation of overpressures typical of paroxysms at Stromboli.

Implications for monitoring

Our results clarify the respective roles of the deep and shallow feeding systems in the initiation of paroxysms. The process starts with the ascent of a LP magma batch from its storage region at 7-10 km depth (Pichavant et al., 2009; Metrich et al., 2010). Timescales are of the order of 1-2 hours maximum for LP magma travel and, although LP magmas all ascend rapidly (u = 1-2 m/s, Fig. 11), there are differences between eruptions. Ascent rates are expected to depend on initial LP melt volatile concentrations and on the gas fraction at depth ((Misiti et al., 2009), both resulting from the deep magmatic evolution. Therefore, u is a parameter essentially fixed deep in the system (assuming steady-state geometries and conditions for the plumbing system). As it is the main N_v controlling variable, the deep feeding system can be considered to govern the textural features of erupted products and the energies of paroxysmal eruptions. The mineralogical and geochemical characteristics of LP magmas also bear the mark of the deep magmatic evolution (e.g., Metrich et al., 2010; Pichavant et al., 2009; 2011; Pompilio et al., 2011). In comparison, LP magma supply rates can vary with either the dynamics of the deep reservoir or feedback effects from the shallow and intermediate parts of the feeding system, alternatively. The main role of the shallow part is to control mechanisms of final LP magma ascent and degassing. Local conditions (temperature, crystallinity, viscosity, permeability and degassing efficiency of the HP magma), structures (volume, 3D geometry of the HP body, location and geometry of conduits) as well as dynamics (lava effusion) can conceivably have an influence, for example by controlling the final ascent velocity and depth of the LP magma column which would either promote or inhibit the evolution toward explosive fragmentation.

This study calls for the development of an integrated monitoring program that looks at the magmatic system as a whole, from deep crustal levels to the surface. On the one hand, imaging in real-time the evolution of the whole plumbing system and in particular the detection of basaltic magma movements in the deep-middle crust appears as a priority given the role of the deep feeding system in the supply of LP magma batches demonstrated here. We are also conscious that monitoring deep-middle portion of the plumbing system implies setting monitoring geophysical networks along the submerged part of the volcanic edifice with all the complications and costs associated. On the other hand, an increasing attention should be given to the shallow seismicity and deformation signals

observed immediately before the 2019 paroxysms (Giudicepietro et al., 2020; Ripepe et al., 2021; Viccaro et al., 2021) because they potentially carry fundamental information on mechanisms of final ascent and overpressurization of the LP magma.

Conclusions

New petrological and textural data have been presented on products from 5 Stromboli paroxysms including the two from 2019 and three historical eruptions (1930, undated and 16th century). Interpretation of the data using experimental simulations constrain timescales of individual mechanisms preceding paroxysms such as LP magma ascent and LP-HP interaction. Results allow paroxysm initiation mechanisms to be discussed and suggestions for monitoring to be formulated. The main findings of this study are the following:

- Paroxysm samples are mixed and include portions representative of both LP and HP magmas. Small but systematic variations in matrix glass major element chemistry are found between samples and eruptions.

- All samples host a population of vesicles ranging from < 15 to > 1000 μm in diameter (on average < 100 μm) and whose size distributions follow mixed exponential to power law behavior. Vesicularities are high (75% on average) and vesicle number densities range from 10^2-10^3 to 10^3-10^4 mm^{-3}. Systematic correlations are observed between vesicle number densities and diameters, and with vesicle growth and nucleation rates as well.

- Using experimental calibrations, the textural data imply average LP magma ascent rates of 1-2 m/s (i.e., ~1.5 hour from 7 to 1.5 km depth). The correlations between ascent rate and vesicle textures demonstrate systematic variations between eruptions. 1930 records the highest vesicle number density and the fastest ascent rate and is the most energetic among the studied paroxysms.

- The near-lack of crystallization during LP magma ascent reflects the small temperature gradient along the decompression path.

- The sieve-textured zones that punctuate growth of plagioclase are markers of mixing and interaction between HP and LP magmas. Experimental calibration of the width of the sieve-textured reaction zone constrains the plagioclase reaction to durations of no more than a few hours.

- Olivine in the HP magma also reacts to the arrival of the LP magma. Experimentally calibrated timescales of the olivine reaction are of the order of a few hours. Phosphorus zonations constrain timescales of olivine crystallization in the HP magma.

- Paroxysm initiation mechanisms such as LP magma ascent and LP-HP interaction are short (in the range of hours). In contrast, paroxysmal eruptions occur as part of longer periods (up to months) of abnormal activity. Arrival of LP magmas at shallow levels is a necessary but not a sufficient condition for a paroxysmal eruption to occur.

- The magma blob model, with possible feedback between the shallow and deep parts of the feeding system, offers the most promising perspectives toward an integrated model of paroxysm initiation at Stromboli. In the frame of this model, the generation of overpressures typical of the highly explosive dynamics of paroxysms is still to be fully elucidated.

- Our results clarify the main respective roles of the deep and shallow feeding system in the initiation of paroxysms, respectively (1) supply of LP magma and (2) control of final degassing of shallow LP magma. The monitoring system should be more dedicated to the detection of basaltic magma movements in the deep-middle crust as well as to geophysical signals indicating an evolution toward explosive degassing of the LP magma.

Acknowledgements

This study was supported by the Labex Voltaire (ANR-10-LABX-100-01), by INGV Progetti Ricerca Libera (Time scale of magma transfer within the Stromboli plumbing system) and by the 'DisEqm' (Quantifying disequilibrium processes in basaltic volcanism) and 'Shedding new light on volcanoes: real time synchrotron X-ray tomography of magmatic phenomena' projects funded by NERC (NE/N018575/1 and NE/M013561/1). Discussions with S. Rotolo helped to design the interaction experiments. E. Deloule is acknowledged for assistance with the SIMS analyses, F. Iacoviello and S. Shah for the tomographic image acquisition and S. Janiec and P. Benoist for the sample preparation. We also acknowledge the use of the X-ray μCT facilities and support provided by Peter D. Lee. The manuscript benefited from stimulating reviews by C. Firth and M. Polacci and editorial advice by S. Vergniolle.

References

Abràmoff, M.D., Magalhães, P.J., Ram, S.J. (2004). Image processing with ImageJ. Biophoton. Int. 11, 36–43.

Aiuppa, A., Federico, C., Giudice, G., Giuffrida, G., Guida, R., Gurrieri, S., Liuzzo, M., Moretti, R., Papale, P. (2009). The 2007 eruption of Stromboli volcano: Insights from real-time measurement of the volcanic gas plume CO_2/SO_2 ratio. J. Volcanol. Geotherm. Res., 182, 221–230.

Aiuppa, A., Burton, M., Caltabiano, T., Giudice, G., Guerrieri, S., Liuzzo, M., Murè, F., Salerno, G. (2010). Unusually large magmatic CO_2 gas emissions prior to a basaltic paroxysm. Geophys. Res. Lett., 37, L17303, doi:10.1029/2010GL043837.

Allard, P. (2010). A CO_2-rich gas trigger of explosive paroxysms at Stromboli basaltic volcano, Italy. J. Volcanol. Geotherm. Res., 189, 363-374.

Andronico D., Del Bello E., Ciancitto F., Cristaldi A., D'Oriano C., Landi P., Pennacchia F., Ricci T., Scarlato P., Taddeucci J. (2020). The 3 July and 28 August 2019 paroxysms at Stromboli. Abstract Volume 4th Conferenza A. Rittmann, p. 243.

Andronico D., Del Bello E., D'Oriano C., Landi P., Pardini F., Scarlato P., de' Michieli Vitturi M., Taddeucci J., Cristaldi A., Ciancitto F., Pennacchia F., Ricci T., Valentini F. (2021). Uncovering the eruptive patterns of the 2019 double paroxysm eruption crisis of Stromboli volcano. Nature Comm. doi.org/10.1038/s41467-021-24420-1.

Bertagnini, A., Métrich, N., Landi, P., Rosi, M. (2003). Stromboli volcano (Aeolian Archipelago, Italy): An open window on the deep-feeding system of a steady state basaltic volcano. Journal of Geophysical Research: Solid Earth, 108, B7, 2336.

Bertagnini, A., Métrich, N., Francalanci, L., Landi, P., Tommasini, S., Conticelli, S. (2008). Volcanology and magma geochemistry of the present-day activity: constraints on the feeding system. In: Calvari, S., Inguaggiato, S., Puglisi, G., Ripepe, M., Rosi, M. (eds) Learning from Stromboli. American Geophysical Union, Washington, Geophysical Monograph, 182, 19–38.

Bertagnini, A., Roberto, A., Pompilio, M. (2011). Paroxysmal activity at Stromboli: lessons from the past. Bull. Volcanol., 73, 1229–1243.

Bevilacqua, A., Bertagnini, A., Pompilio, M., Landi, P., Del Carlo, P., Di Roberto, A., Aspinall, W., Neri, A. (2020). Major explosions and paroxysms at Stromboli (Italy): a new historical catalog and temporal models of occurrence with uncertainty quantification. Sci. Reports, 10, 17357.

Calvari S., Spampinato, L., Lodato, L. (2006). The 5 April 2003 Vulcanian paroxysmal explosion at Stromboli volcano (Italy) from field observations and thermal data. J. Volcanol. Geotherm. Res., 149, 160-175.

Calvari, S., Spampinato, L., Bonaccorso, A., Oppenheimer, C., Rivalta, E., Boschi, E., (2011). Lava effusion–A slow fuse for paroxysms at Stromboli volcano? Earth Planet. Sci. Lett., 301, 317–323.

Cashman, K.V., Mangan, M.T. (1994). Physical aspects of magmatic degassing II. Constraints on vesiculation processes from textural studies of eruptive products. Rev. Mineral. 30, 447-478.

Di Carlo, I., Pichavant, M., Rotolo, S., Scaillet, B. (2006). Experimental crystallization of a high-K arc basalt: the golden pumice, Stromboli volcano (Italy). J. Petrol., 47, 1317-1343.

Di Carlo, I., Pichavant, M., Rotolo, S., Scaillet, B. (2010). Textures and kinetics of mineral-melt reactions in volatile-bearing basaltic melts. EMPG XIII Toulouse Abstract volume, p. 54.

Di Roberto, A., Bertagnini, A., Pompilio, M., Bisson, M. (2014). Pyroclastic density currents at Stromboli volcano (Aeolian Islands, Italy): a case study of the 1930 eruption. Bull. Volcanol., 76:827, doi10.1007/s00445-014-0827-5.

Di Stefano, F., Mollo, S., Ubide, T., Petrone, C.M., Caulfield, J., Scarlato, P., Nazzari, M., Andronico, D., Del Bello, E. (2020). Mush cannibalism and disruption recorded by clinopyroxene

phenocrysts at Stromboli volcano: New insights from recent 2003–2017 activity. Lithos, 360-361, 105440.

D'Oriano, C., Bertagnini, A., Pompilio, M. (2011). Ash erupted during normal activity at Stromboli (Aeolian Islands, Italy) raises questions on how the feeding system works. Bull. Volcanol., 73, 471-477.

Giordano, G., De Astis, G. (2021). The summer 2019 basaltic Vulcanian eruptions (paroxysms) of Stromboli. Bull. Volcanol., 83, 1, doi-org.insu.bib.cnrs.fr/10.1007/s00445-020-01423-2.

Giudicepietro, F., López, C., Macedonio, G., Alparone, S., Bianco, F., Calvari, S., De Cesare, W., Delle Donne, D., Di Lieto, B., Esposito, A.M., Orazi, M., Peluso, R., Privitera, E., Romano, P., Scarpato, G., Tramelli, A. (2020). Geophysical precursors of the July-August 2019 paroxysmal eruptive phase and their implications for Stromboli volcano (Italy) monitoring. Sci. Reports, 10, doi.org/10.1038/s41598-020-67220-1.

Hammouda, T., Pichavant, M. (2000). Melting of fluorphlogopite-plagioclase pairs at 1 atm. Eur. J. Mineral., 12, 315-328.

Houghton, B.F., Gonnermann, H.M. (2008). Basaltic explosive volcanism: constraints from deposits and models. Chem. Erde, 68, 117-140.

James, M.R., Lane, S.J., Corder, S.B. (2008). Modelling the rapid near-surface expansion of gas slugs in low-viscosity magmas. In: Lane, S.J., Gilbert, J.S. (eds) Fluid motions in volcanic conduits: A source of seismic and acoustic signals. Geological Society, London, Special Publications, 307, 147–167.

Jarosewich E., Nelen, J.A., Norberg, J.A. (1980). Reference samples for electron microprobe analysis. Geostandards Newslett., 4, 43–47.

Landi, P., Métrich, N., Bertagnini, A., Rosi, M. (2004). Dynamics of magma mixing and degassing recorded in plagioclase at Stromboli (Aeolian Archipelago, Italy). Contrib. Mineral. Petrol., 147, 213–227.

Landi, P., Francalanci, L., Pompilio, M., Rosi, M., Corsaro, R.A., Petrone, C.M., Nardini, I., Miraglia, L. (2006). The December 2002-July 2003 effusive event at Stromboli volcano, Italy: insights into the shallow plumbing system by petrochemical studies. J. Volcanol. Geotherm. Res., 155, 263-284.

Landi P., Corsaro, R.A., Francalanci L., Civetta L., Miraglia L., Pompilio M., Tesoro R. (2009). Magma dynamics during the 2007 Stromboli eruption (Aeolian Islands. Italy): mineralogical, geochemical and isotopic data. J Volcanol Geotherm Res., 182, 255-268.

Le Gall, N., Pichavant, M. (2016a). Homogeneous bubble nucleation in H_2O- and H_2O-CO_2-bearing basaltic melts: results of high temperature decompression experiments. J. Volcanol. Geotherm. Res., 327, 604-621.

Le Gall, N., Pichavant, M. (2016b). Experimental simulation of bubble nucleation and magma ascent in basaltic systems: Implications for Stromboli volcano. Am. Mineral., 101, 1967-1987.

Mangan, M.T., Cashman, K.V., Newman, S. (1993). Vesiculation of basaltic magma during eruption. Geology, 21, 157-160.

Massol, H., Jaupart, C. (1999). The generation of gas overpressure in volcanic eruptions. Earth Planet. Sci. Lett., 166, 57-70.

Massol, H., Koyaguchi, T. (2005). The effect of magma flow on nucleation of gas bubbles in a volcanic conduit. J. Volcanol. Geotherm. Res., 143, 69–88.

Métrich, N., Bertagnini, A., Landi, P., Rosi, M. (2001). Crystallization driven by decompression and water loss at Stromboli volcano (Aeolian Islands, Italy). J. Petrol., 42, 1471–1490.

Métrich, N., Bertagnini A., Di Muro, A. (2010) Conditions of magma storage, degassing and ascent at Stromboli: new insights into the volcanic plumbing system with inferences on the eruptive dynamics. J. Petrol., 51, 603-626.

Métrich, N., Bertagnini A., Pistolesi, M. (2021). Paroxysms at Stromboli volcano (Italy): source, genesis and dynamics. Front. Earth Sci. 9:593339. doi: 10.3389/feart.2021.593339.

Masotta, M., Pontesilli, A., Mollo, S., Armienti, P., Ubide, T., Nazzari, M., Scarlato, P. (2020). The role of undercooling during clinopyroxene growth in trachybasaltic magmas: Insights on magma decompression and cooling at Mt. Etna volcano. Geochim. Cosmochim. Acta, 268, 258-276.

Misiti, V., Vetere, F., Mangiacapra, A., Behrens, H., Cavallo, A., Scarlato, P., Dingwell, D.B. (2009). Viscosity of high-K basalt from the 5th April 2003 Stromboli paroxysmal explosion. Chem. Geol., 260, 278–285.

Nakamura, M., Shimakita, S. (1998). Dissolution origin and syn-entrapment compositional change of melt inclusion in plagioclase. Earth Planet. Sci. Lett., 161, 119-133.

Namiki, A., Manga, M. (2006). Influence of decompression rate on the expansion velocity and expansion style of bubbly fluids. J. Geophys. Res., 111, B11208, doi:10.1029/2005JB004132.

Navon, O., Lyakhovsky, V. (1998). Vesiculation processes in silicic magmas, In: Gilbert, J.S, Sparks, R.S.J. (eds) The Physics of Explosive Volcanic Eruptions. Geological Society, London, Special Publications, 145, 27-50.

Nishiwaki, M., Toramaru, A. (2019). Inclusion of viscosity into classical homogeneous nucleation theory for water bubbles in silicate melts: reexamination of bubble number density in ascending magmas. J. Geophys. Res., 124, 8250–8266. doi.org/10.1029/2019JB017796.

Parfitt, E.A. (2004). A discussion of the mechanisms of explosive basaltic eruptions. J. Volcanol. Geotherm. Res., 134, 77-107.

Petrone, C.M., Braschi, E., Francalanci, L., Casalini, M., Tommasini, S. (2018). Rapid mixing and short storage timescale in the magma dynamics of a steady-state volcano. Earth Planet. Sci. Lett., 492, 206–221.

Pichavant, M., Di Carlo, I., Le Gac, Y., Rotolo, S., Scaillet, B. (2009). Experimental constraints on the deep magma feeding system at Stromboli volcano, Italy. J. Petrol., 50, 601-624.

Pichavant, M., Pompilio, M., d'Oriano, C., Di Carlo, I. (2011). Petrography, mineralogy and geochemistry of a primitive pumice from Stromboli: implications for the deep feeding system; Eur. J. Mineral., 23, 499-517.

Pichavant, M., Di Carlo, I., Rotolo, S.G., Scaillet, B., Burgisser, A., Le Gall, N., Martel, C. (2013). Generation of CO_2-rich melts during basalt magma ascent and degassing. Contrib. Mineral. Petrol., 166, 545–561.

Pichavant, M., Le Gall, N., Scaillet, B. (2019). Gases as precursory signals: experimental simulations, new concepts and models of magma degassing. Advs in Volcanology, 139–154 doi 10.1007/11157_2018_35.

Pichavant, M., Di Carlo, I., Pompilio, M., Le Gall, N. (2020). Experimental simulation of ascent and fragmentation of Stromboli LP magmas. Abstract Volume 4th Conferenza A. Rittmann, p. 139.

Pioli, L., Pistolesi, M., Rosi, M. (2014). Transient explosions at open-vent volcanoes: the case of Stromboli (Italy). Geology, 42, 863-866.

Pistolesi, M., Rosi, M., Pioli, L., Renzulli, A., Bertagnini, A., Andronico, D. (2008). The paroxysmal event and its deposits. In: AGU, Geophysical Monograph 182, Washington, DC, 317–330.

Pistolesi, M., Delle Donne, D., Pioli, L., Rosi, M., Ripepe, M. (2011). The 15 March 2007 explosive crisis at Stromboli volcano, Italy: assessing physical parameters through a multidisciplinary approach. J. Geophys. Res., 116, B12206, doi:10.1029/2011JB008527.

Polacci, M., Baker, D.R., Mancini, L., Tromba, G., Zanini, F. (2006). Three-dimensional investigation of volcanic textures by X-ray microtomography and implications for conduit processes. Geophys. Res. Lett., 33, L13312, doi:10.1029/2006GL026241.

Polacci, M., Baker, D.R., Mancini, L., Favretto, S., Hill, R.J. (2009). Vesiculation in magmas from Stromboli and implications for normal Strombolian activity and paroxysmal explosions in basaltic systems. Journal of Geophysical Research: Solid Earth, 114, B01206.

Pompilio, M., Bertagnini, A., Métrich, N. (2011). Geochemical heterogeneities and dynamics of magmas within the plumbing system of a persistently active volcano: evidence from Stromboli. Bull. Volcanol. 64, 171–194.

Proussevitch, A.A., Sahagian, D.L., Anderson, A.T. (1993). Dynamics of diffusive bubble growth in magmas: isothermal case. Journal of Geophysical Research 98, 22,283-22,307.

Proussevitch, A.A., Sahagian, D.L., Tsentalovich, E.P. (2007). Statistical analysis of bubble and crystal size distributions: formulations and procedures. J. Volcanol. Geotherm. Res. 164, 95–111.

Rosi, M., Pistolesi, M., Bertagnini, A., Landi, P., Pompilio, M., Di Roberto, A. (2013). Stromboli volcano, Aeolian Islands (Italy): present eruptive activity and hazards. Geological Society, London, Memoirs, 37, 473–490.

Ripepe, M., Pistolesi, M., Coppola, D., Delle Donne, D., Genco, R., Lacanna, G., Laiolo, M., Marchetti, E., Ulivieri, G., Valade, S. (2017). Forecasting effusive dynamics and

decompression rates by magmastatic model at open-vent volcanoes. Sci. Reports 7: 3885 doi:10.1038/s41598-017-03833-3.

Ripepe, M., Lacanna, G., Pistolesi, M., Silengo, M.C., Aiuppa, A., Laiolo, M., Massimetti, F., Innocenti, L., Della Schiava, M., Bitetto, M., La Monica, F.P., Nishimura, T., Rosi, M., Mangione, D, Ricciardi, A., Genco, R., Coppola, D., Marchetti, E., Delle Donne, D. (2021). Ground deformation reveals the scale-invariant conduit dynamics driving explosive basaltic eruptions. Nature Com.,12:1683 doi.org/10.1038/s41467-021-21722-2.

Shea, T. (2017). Bubble nucleation in magmas: A dominantly heterogeneous process ? J. Volcanol. Geotherm. Res. 343, 155–170.

Shea, T., Hammer, J.E., Hellebrand, E., Mourey, A.J., Costa, F., First, E.C., Lynn, K.J., Melnik, O. (2019). Phosphorus and aluminum zoning in olivine: contrasting behavior of two nominally incompatible trace elements. Contrib. Mineral. Petrol., 174, 85.

Sparks, R.S.J. (1978). The dynamics of bubble formation and growth in magmas: a review and analysis. J. Volcanol. Geotherm. Res., 3, 1–37.

Sparks, R.S.J., Barclay, J., Jaupart, C., Mader, H.M., Phililips, J.C. (1994). Physical aspects of magmatic degassing I. Experimental and theoretical constraints on vesiculation. Rev. Mineral. 30, 413-445.

Toramaru, A. (1995). Numerical study of nucleation and growth of bubbles in viscous magmas. J. Geophys. Res., 100, B2, 1913-1931.

Toramaru, A. (2006). BND (bubble number density) decompression rate meter for explosive volcanic eruptions. J. Volcanol. Geotherm. Res. 154, 303–316.

Tsuchiyama, A. (1985). Dissolution kinetics of plagioclase in the melt of the system diopside-albite-anorthite, and origin of dusty plagioclase in andesites. Contrib. Mineral. Petrol., 89, 1–16.

Tsuchiyama, A., Takahashi, E. (1983). Melting kinetics of a plagioclase feldspar. Contrib. Mineral. Petrol., 84, 345–354.

Ubide, T., Caufield, J., Brandt, C., Bussweiler, Y., Mollo, S., Di Stefano, F., Nazarri, M., Scarlato, P. (2019). Deep magma storage revealed by multi-method elemental mapping of clinopyroxene megacrysts at Stromboli volcano. Sci. Reports, 7, 239.

Vergniolle, S., Brandeis, G. (1996). Strombolian explosions 1. A large bubble breaking at the surface of a lava column as a source of sound. J. Geophys. Res., 101, B9, 20433-20447.

Vergniolle, S., Brandeis, G., Mareschal, J.-C. (1996). Strombolian explosions 2. Eruption dynamics determined from acoustic measurements. J. Geophys. Res., 101, B9, 20449-20466.

Vergniolle, S., Gaudemer, Y. (2015). From reservoirs and conduits to the surface: Review of role of bubbles in driving basaltic eruptions. In: Carey, R., Cayol, V., Poland, M. and Weis, D. (eds) Hawaiian volcanoes: from source to surface. Geophysical Monograph 208, 289-321.

Vicarro, M., Cannata, A., Cannavò, F., De Rosa, R., Giuffrida, M., Nicotra, E., Petrelli, M., Sacco, G. (2021). Shallow conduit dynamics fuel the unexpected paroxysms of Stromboli volcano during the summer 2019. Sci. Reports, 11, 266.

Zhang Y., Ni H. (2010) Diffusion of H, C, and O components in silicate melts. In: Zhang Y., Cherniak D.J. (eds) Diffusion in Minerals and Melts. Mineralogical Society of America Reviews in Mineralogy 72, pp 171-225.

Figure Captions

Fig. 1. View of Stromboli volcano and main sampling localities (image from Google Earth). Stars refer to location of stratigraphic sections in which samples of 1930, 16th century and undated (PST-9) eruptions have been collected. Area A represent sampling sites of lapilli produced during the July 3 2019 eruption; B is the sampling area of large spatter bombs erupted on July 3 2019; C is the sector were lapilli and bombs erupted on August 28 2019 have been collected. See also Table S1.

Fig. 2. Major element compositions of matrix glasses. All data are from this study except for PST-9 (Pichavant et al., 2011). Representative compositions are reported in Table S2. Literature data are from Metrich et al. (2010) for LP and from Landi et al. (2006) for HP matrix glasses. Note that LP and HP compositions are plotted with the same symbol.

Fig. 3. Example of textural and compositional zonation in type (1) plagioclase (PST 238, 16th century eruption). (a) SEM image of the crystal. (b) Electron microprobe Ca Kα X-ray distribution map. (c) Results of the electron microprobe profile A-B shown in (b). Notice the complex sieve-textured core and the two An-rich sieve-textured zones separated by a homogeneous An ~65 overgrowth. The internal sieve texture zone has a thickness of ~100 μm whereas the external is narrower.

Fig. 4. Plagioclase reaction textures. (a) SEM image of plagioclase reaction zone in experimental charge R5-4 (Table 2). A continuous reaction zone of width d_{plag} rims the crystal. See Tsuchiyama and Takahashi (1983), Tsuchiyama (1985), Nakamura and Shimakita (1998) and Hammouda and Pichavant (2000) for similar experimental plagioclase reaction textures. The image on the right is an enlarged view of the zone (marked by the white square) at the left. Dissolution of initial plagioclase (An 68) is accompanied by crystallization of a new more calcic (An 84-85) plagioclase. Notice the skeletal texture of the new plagioclase in the outer part of the reaction rim and the white layers surrounding the new plagioclase indicating accumulation of Fe at the front of the growing crystal. (b) electron microprobe Fe Kα X-ray map of (a). (c) Plagioclase reaction texture in sample PST-9 (Pichavant et al., 2011). Notice the textural and compositional similarity between experimental (a, b) and natural (c) plagioclase.

Fig. 5. Example of textural and compositional zonation in type (5) olivine crystal 1B (Fo 69.5-70.3, Table S3) from sample PST 2019-1 (July 2019 eruption). (a) SEM image of the crystal. The inset at left is an enlargement of the zone marked by the white square. (b) Electron microprobe P Kα X-ray distribution map of (a). (c) Results of the electron microprobe profile A-B shown in (b). Note the fine oscillatory P growth zoning in the crystal which comprises two parts, an inner and an external zone separated by a reaction zone (~150 μm thick) marked by numerous zonally disposed glass inclusions (inset in (a)) and low P concentrations (below the P detection limit, ~40 ppm). The glass rimming the crystal is P-rich.

Fig. 6. Representative textures of transformation of type (5) olivine. All SEM images are from minerals separated from sample PST 239 (1930 eruption). Panels (a), (b) to (c) illustrate the progressive transformation of olivine as a result of interaction with the LP magma. (a): incipient transformation, only a narrow rim of Fo-rich olivine has developed and the reaction zone is restricted to a few areas at the edge of the crystal. (b): more advanced transformation, the reaction zone forms a continuous layer around the crystal and the narrow Fo-rich rim is in external position, in contact with the glass. Notice the appearance of small melt inclusions in the reaction zone (white arrow). The large melt inclusions in the center are remnants of an earlier, now fossil, reaction. (c): extensive transformation, the reaction zone has invaded most of the crystal and the unreacted part is limited to the central part. Notice the thin external Fo-rich zone, the large melt inclusions in the reaction zone (white arrow) and the diffuse and patchy zonation in the reaction zone. A few small (< 5 μm) Ti-magnetites are also present. The end product of the transformation is a chemically heterogeneous crystal, reversely and patchily zoned with a Fo-rich layer zone mantling the homogeneous Fo-poor core, similar to a type (4) olivine.

Fig. 7. Extensive experimental olivine reaction texture. The initial crystal is texturally and compositionally similar to olivine 1B in Fig. 5a. (a) SEM image of olivine reaction in charge R2-7 (Table 2). A continuous reaction zone of variable width (d_{ol}) rims the crystal. Olivine in the reaction zone shows a patchy texture, progressively evolving from Fo71 (core) to Fo88 (outer rim). The reaction zone contains melt inclusions outlined by the white arrow, some with Fe oxides (magnetites) daughter crystals. (b) electron microprobe P Kα X-ray map. The olivine growth zonation in the core of the crystal is sharply crosscut by the experimentally induced reaction zone. Notice the abundance of melt inclusions and the low P concentrations in the reaction zone.

Fig. 8. Representative 3D volumes of pumice clasts. (a) August 2019 (PST 2019-8), (b) July 2019 (PST 2019-4) and (c) 16th century (PST 12LP). Vesicles appear in black, melt as bright interstitial domains and crystals as rare white objects in PST 2019-4 and PST 2019-8.

Fig. 9. Cumulative vesicle size distribution (VSD) in natural samples. Data from this study and from Polacci et al. (2009) for the 2003 and 2007 samples. The vesicle distribution in an experimental sample (series 2, D8#2, P_{fin} = 25 MPa, u = 1.5 m/s, Le Gall and Pichavant, 2016b) is also shown for comparison. See text and Table 3.

Fig. 10. Comparison between natural and experimental vesicle textures. Data in Table 3 for natural samples and from Le Gall and Pichavant (2016a; b) and Pichavant et al. (2013) for experimental samples at 1200°C and 1150°C respectively. The PST 2019-8 sample is labelled with an asterisk because this sample is texturally specific (see text). (a) vesicle number densities (N_v, mm^{-3}) vs. decompression rate (ascent velocity, u, m/s) for constant P_{fin} (pressure of final ascent), either 50 or 25 MPa. The error bar is the average uncertainty for the natural samples (Table 3). (b) vesicle number densities (N_v, mm^{-3}) vs. P_{fin} (MPa) for constant u, either 1.5 or 3 m/s. Note that the 1150°C point is for u = 1 m/s. (c) Average diameter of the vesicle population (D_{av}, µm) vs. decompression rate (ascent velocity, u, m/s) for constant P_{fin} (pressure of final ascent), either 50 or 25 MPa. The error bar is the average uncertainty for the natural samples (Table 3). The D range for the 2003 eruption is shown but not considered in the interpretations (see text). (d) Average diameter of the vesicle population (D_{av}, µm) vs. P_{fin} (MPa) for constant u, either 1.5 or 3 m/s. Note that the 1150°C point is for u = 1 m/s. Experimental errors for the 1.5 m/s data points are shown (Le Gall and Pichavant, 2016b).

Fig. 11. (a) Ascent velocities (u, m/s) for Stromboli magmas. Black symbols: geophysical/ volcanological estimates; grey symbols: petrological estimates. (1) Constrained from natural and experimental vesicle textures (this study). (2) Calculated from viscosity data and ascent model (Misiti et al., 2009). (3) Calculated from observed volume fluxes and vent areas (rise speeds, Parfitt, 2004); (4) Calculated from magma volumes and model (Calvari et al., 2011); (5) Calculated from gravity-driven eruption model (Ripepe et al., 2017). (6) Calculated from ground deformation model (Ripepe et al., 2021). (b) Timescales (h) for LP-HP magma interaction. All data from this study. Right-pointing arrows indicate minimum durations and left-pointing maximum durations. See text.

Figure1

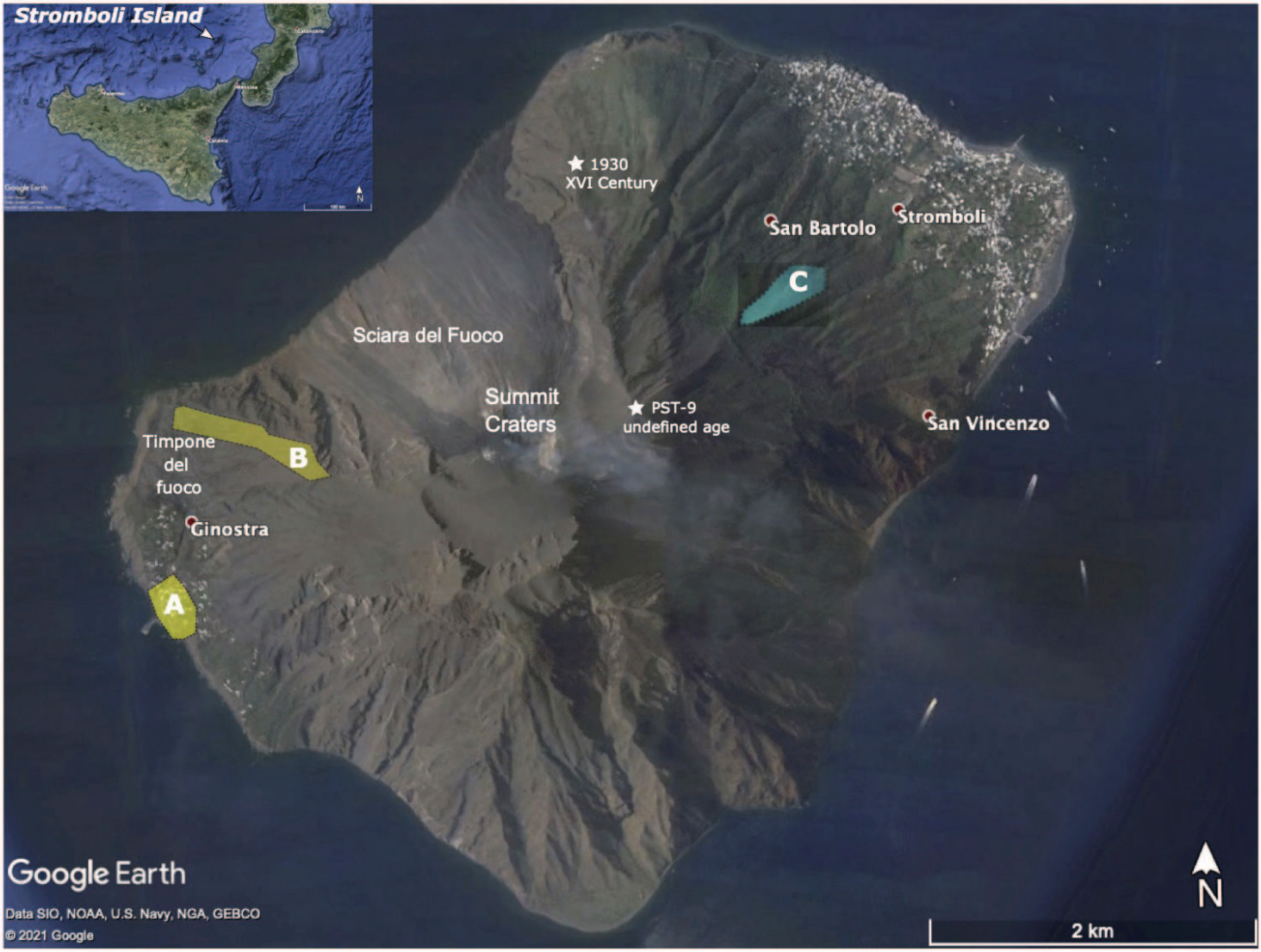

Pichavant et al. Fig. 1

Figure2

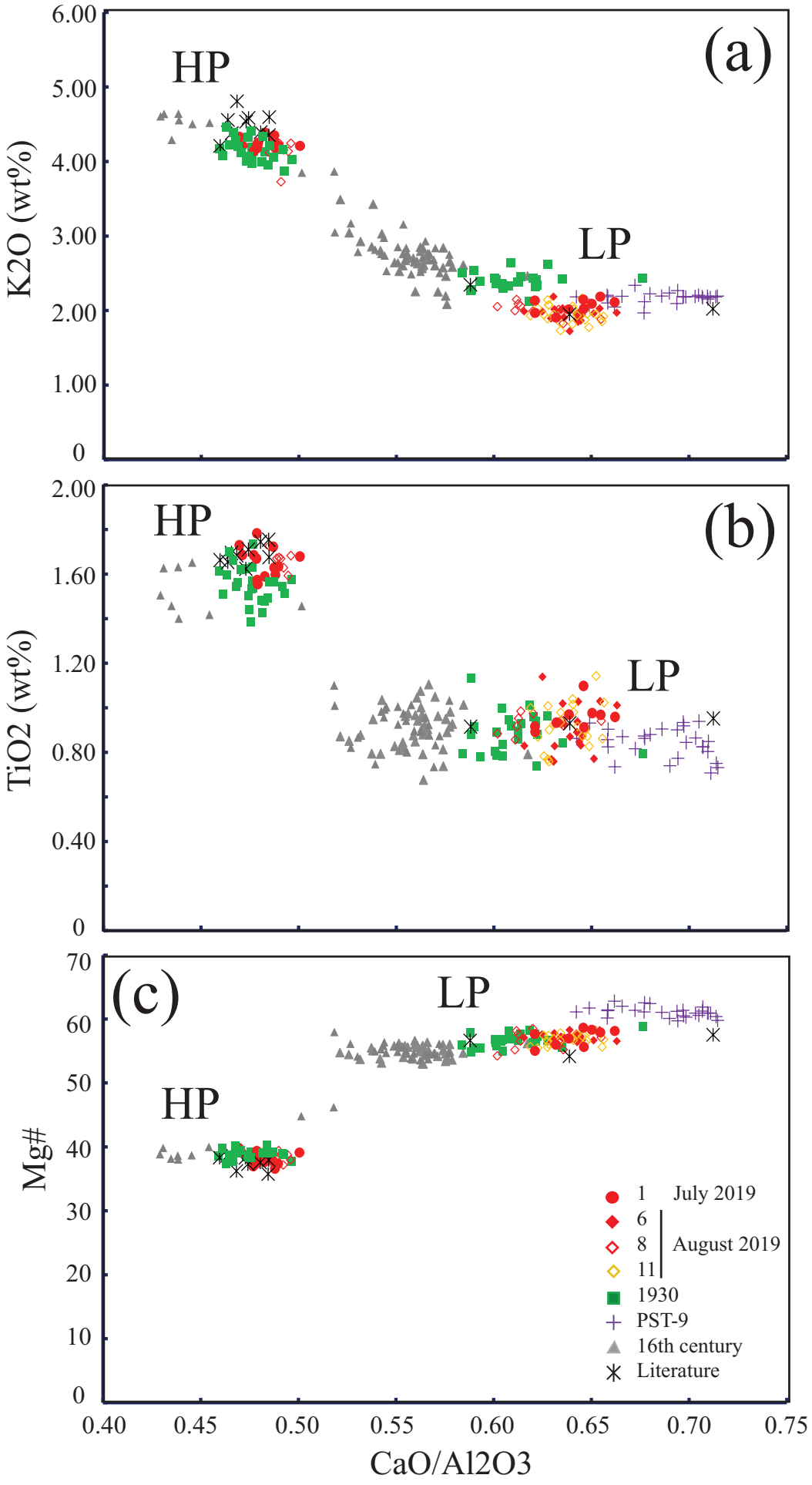

Pichavant et al. Fig. 2

Figure3

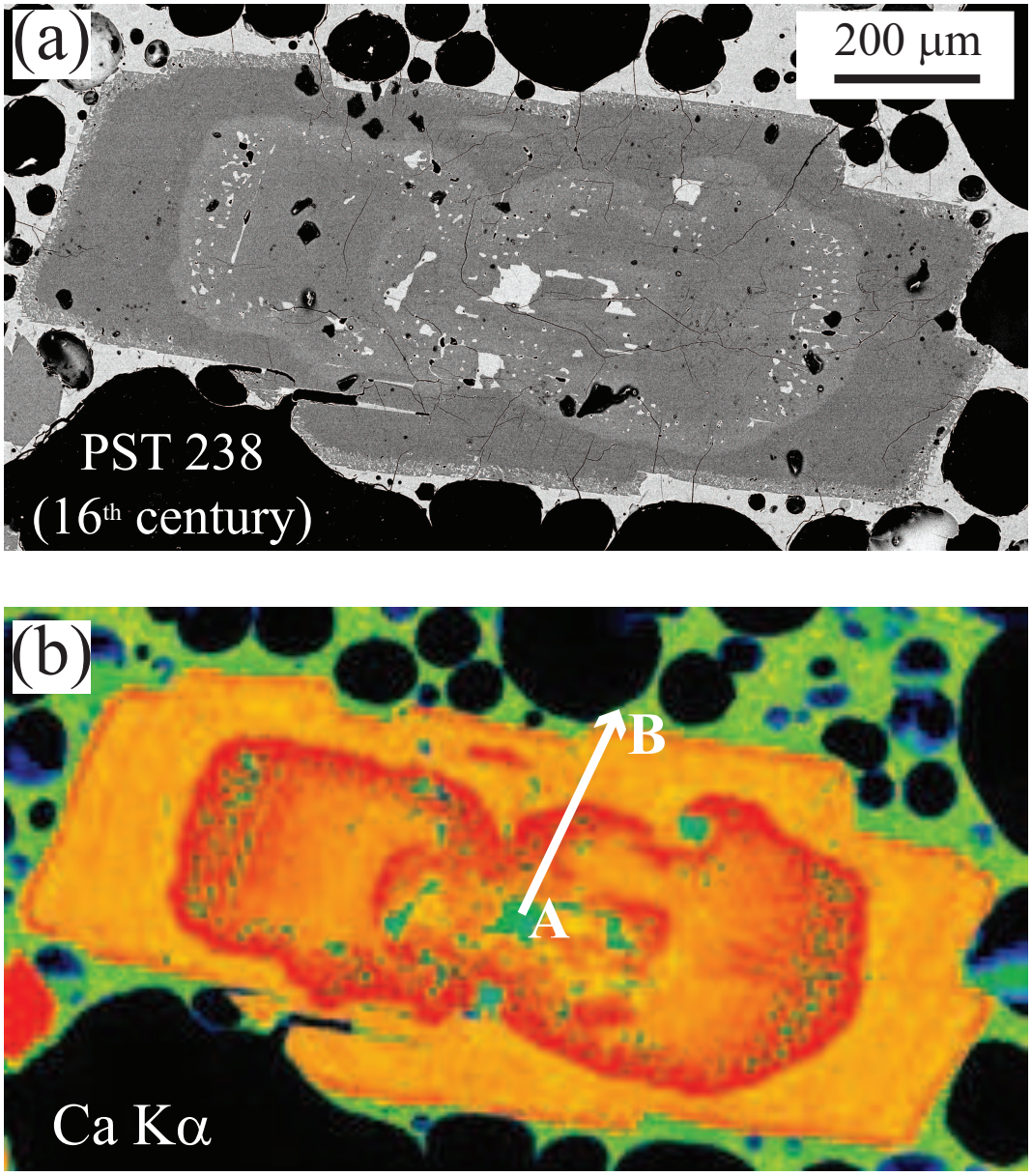

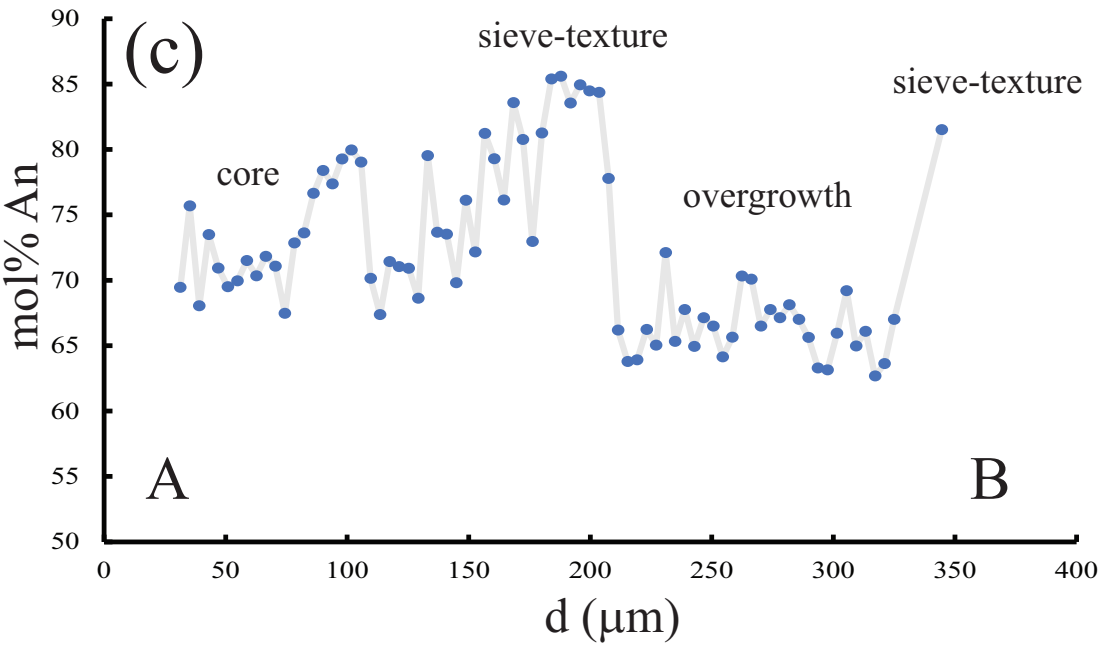

Pichavant et al. Fig. 3

Figure4

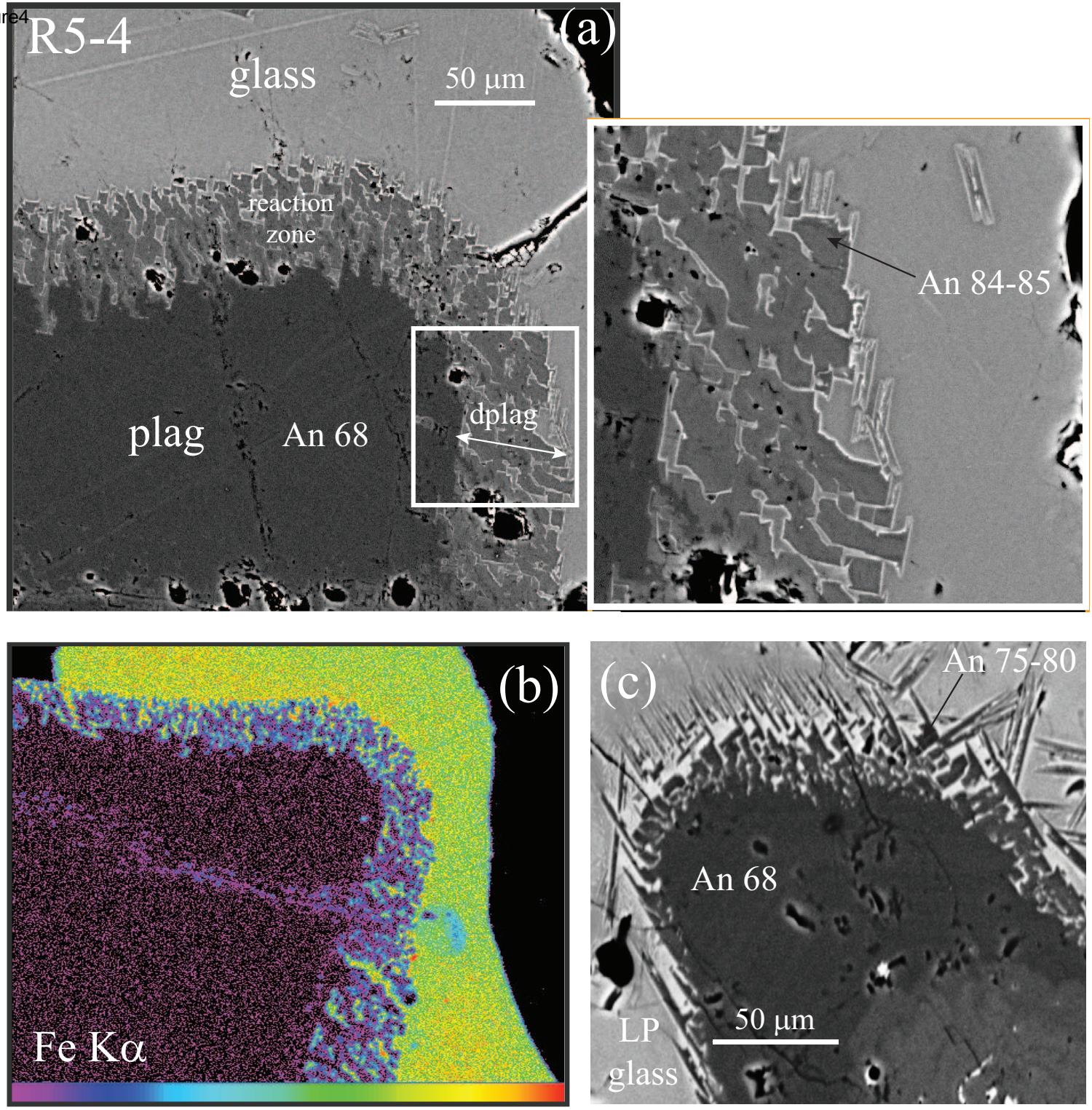

Pichavant et al. Fig. 4

Figure5

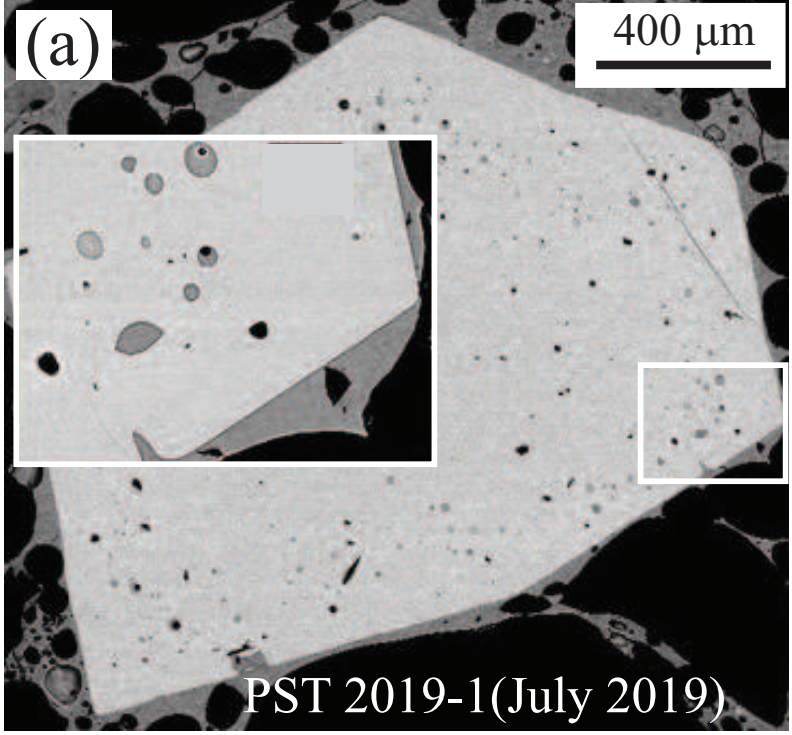

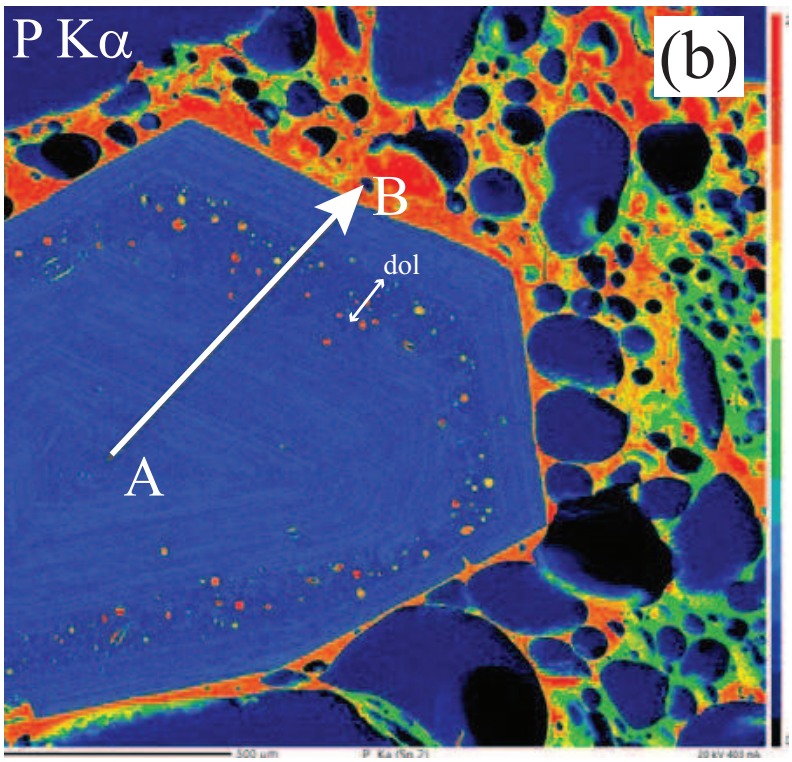

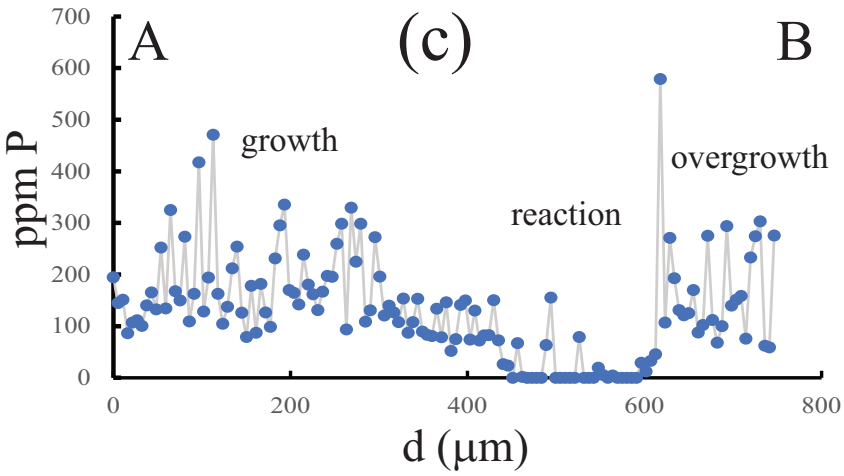

Pichavant et al. Fig. 5

Figure6

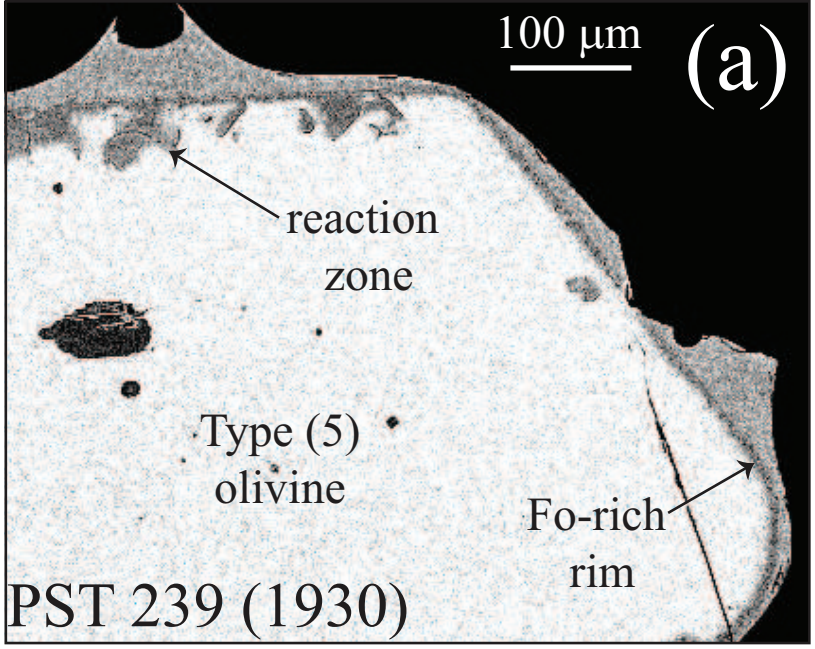

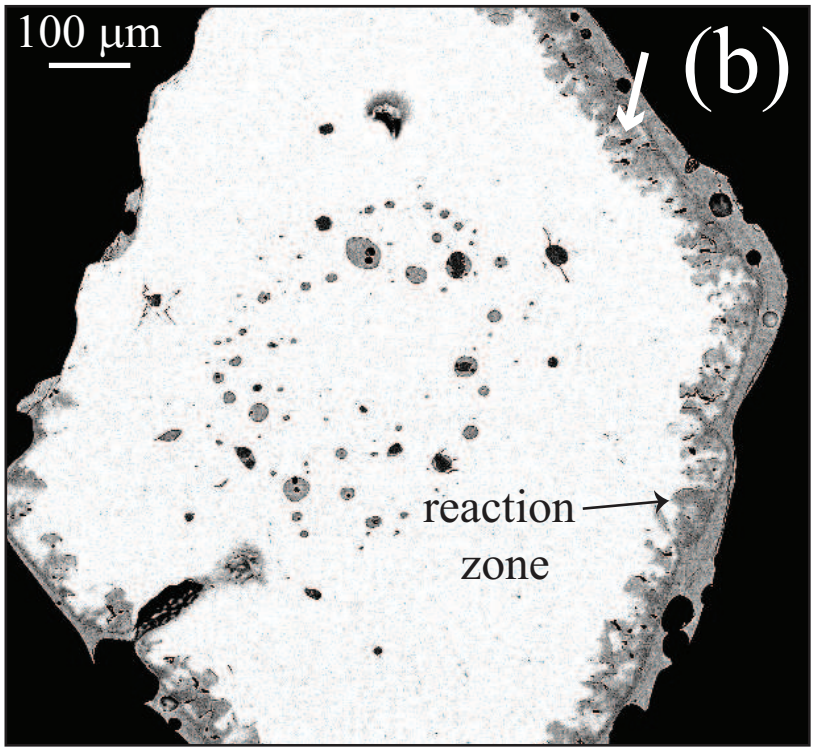

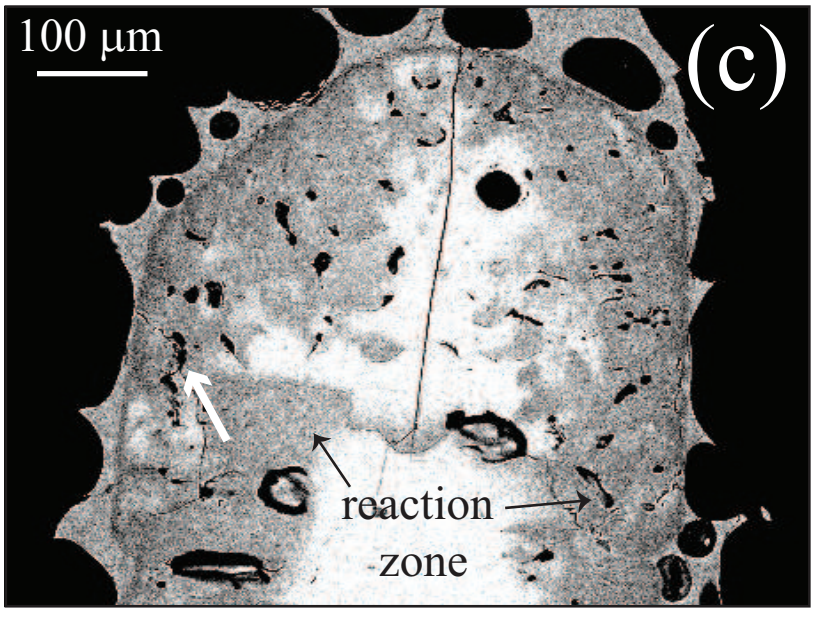

Pichavant et al. Fig. 6

Figure7

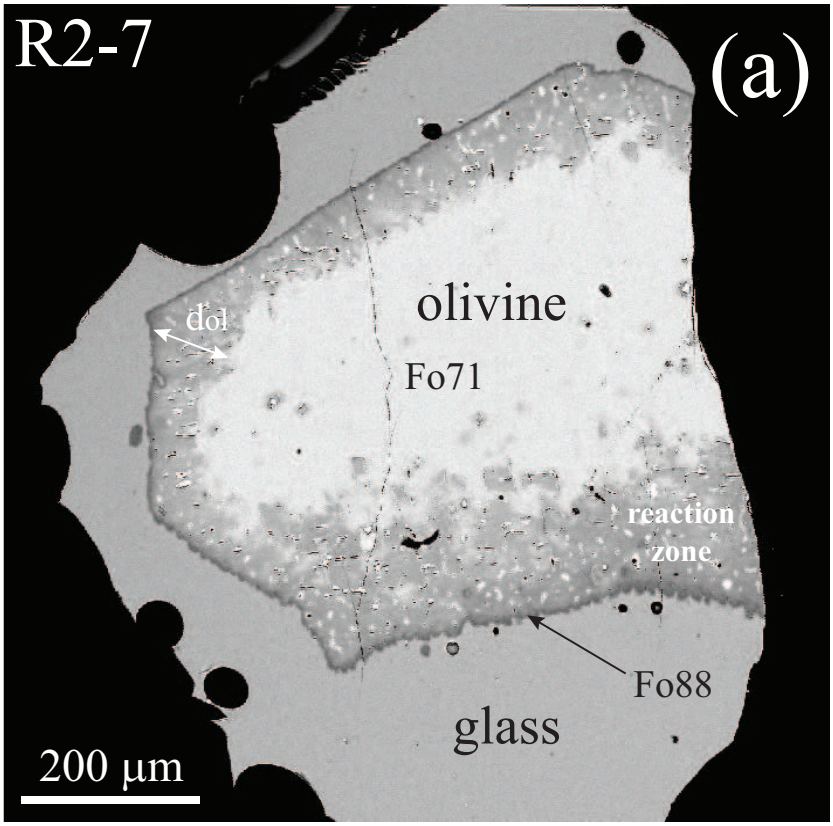

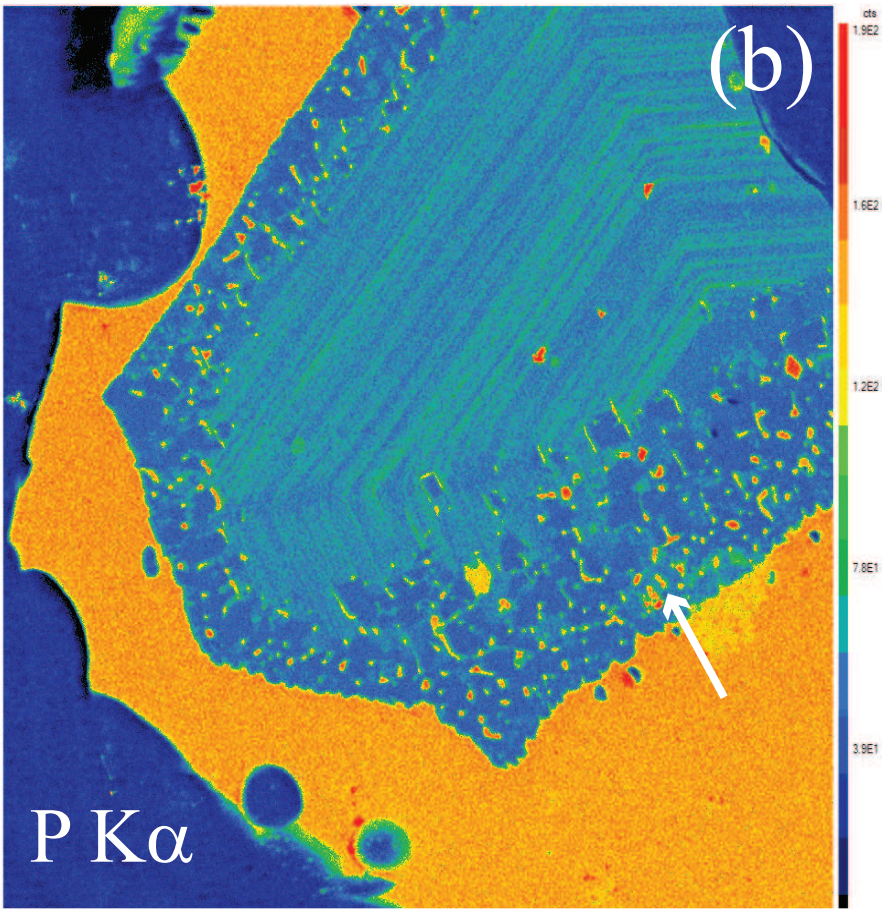

Pichavant et al. Fig. 7

Figure8

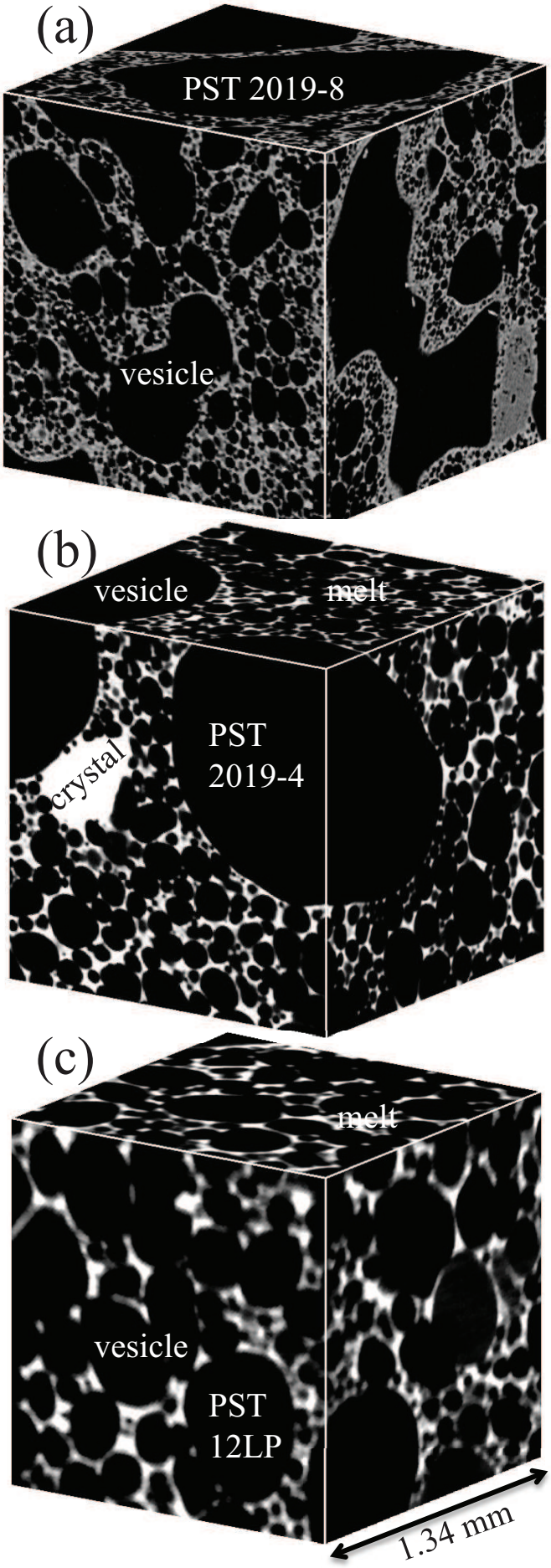

Pichavant et al. Fig. 8

Figure9

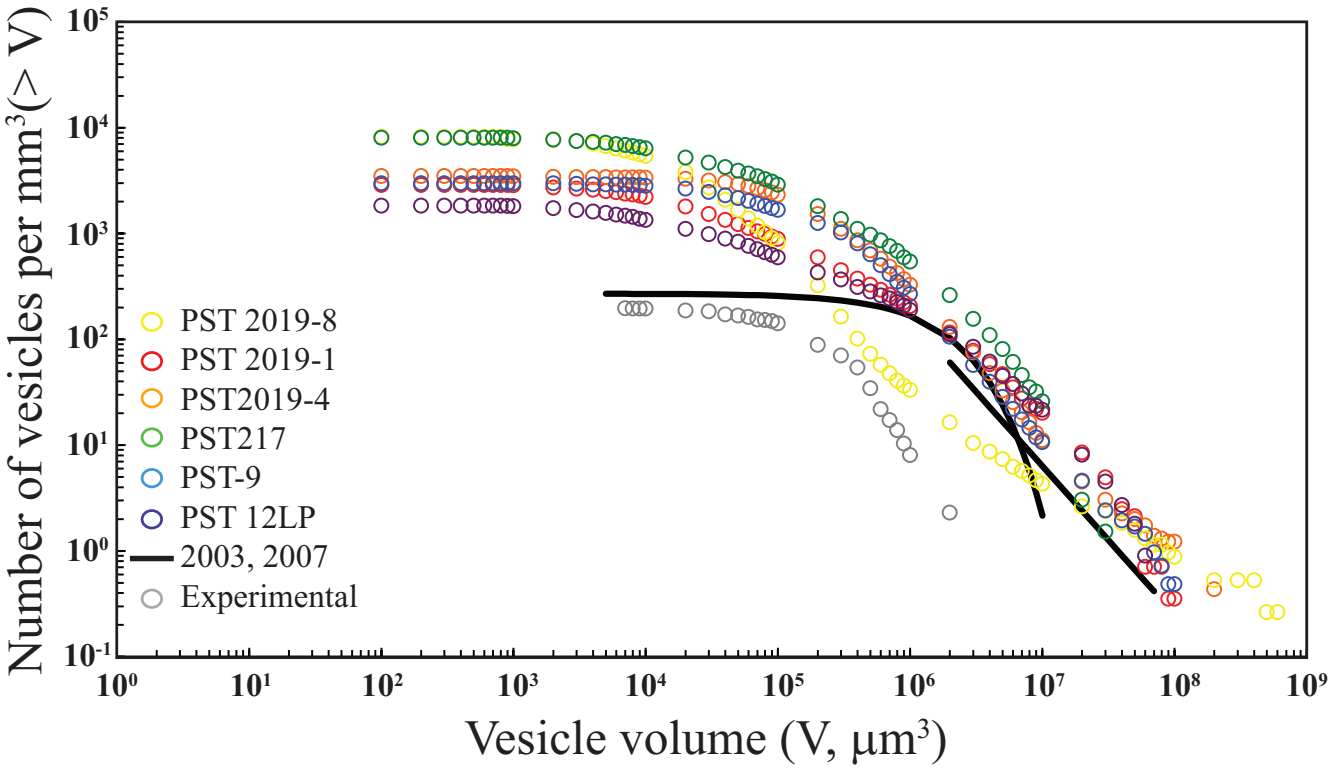

Pichavant et al. Fig.

Figure 10

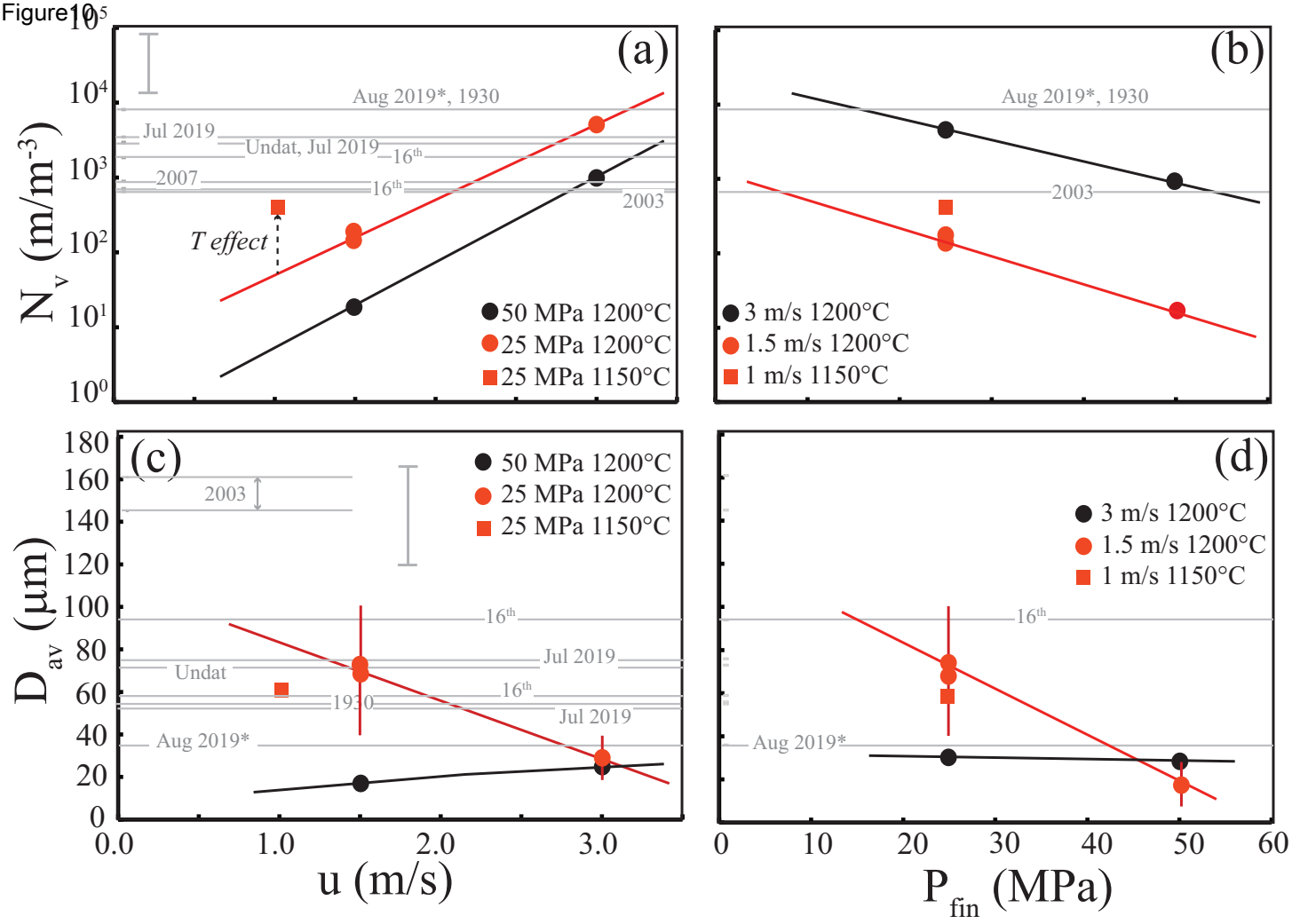

Pichavant et al. Fig. 10

Figure11

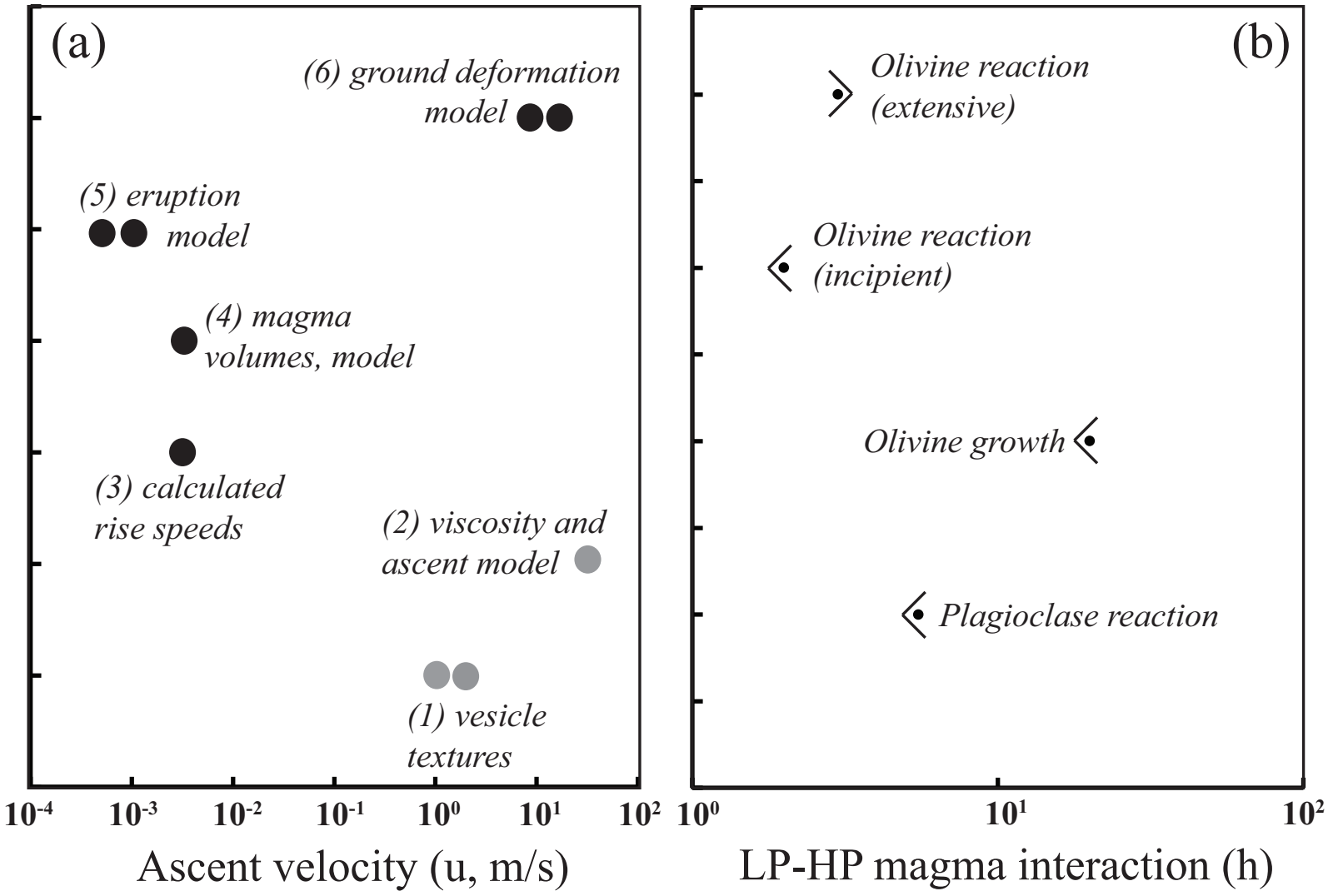

Pichavant et al. Fig. 11

Table1

Table 1. Summary of petrological characteristics of LP magma samples

Paroxysm	Sample	Magma		Ol type					Cpx type					Plag type	
		LP (%)[a]	HP (%)	1 (%)[b]	2 (%)	3 (%)	4 (%)	5 (%)	1 (%)	2 (%)	3 (%)	4 (%)	5 (%)	1 (%)	2 (%)
August 2019	PST2019-6	40	60	nd	nd	nd	nd	nd	nd	nd	nd	nd	nd	nd	nd
	PST2019-8	70	30	7	0	13	27	53	36	4	0	40	20	80	20
	PST2019-10	90	10	0	0	0	0	100	0	0	0	57	43	100	0
	PST2019-11	>90	<10	nd	nd	nd	nd	nd	nd	nd	nd	nd	nd	nd	nd
July 2019	PST2019-1	60	40	11	11	22	0	56	25	13	0	31	31	75	25
	PST2019-4	50	50	nd	nd	nd	nd	nd	nd	nd	nd	nd	nd	nd	nd
	PST2019-5	40	60	0	0	0	0	100	0	0	0	14	86	100	0
1930	PST239	80	20	6	8	22	44	19	18	27	13	27	16	72	28
Undated	PST-9	>90	<10	30	30	9	13	17	50	21	29	0	0	75	25
16th century	PST238	>90	<10	3	12	24	33	27	8	15	0	77	0	75	25

[a] Proportions determined from SEM panoramas of polished samples.
[b] Proportions determined from mineral separates.
LP: low-porphyricity; HP: high-porphyricity; Ol: olivine; Cpx: clinopyroxene; Plag: plagioclase.
nd: not determined.
See Supplementary Material and text for the definition of mineral types and interpretations.

Table 2. Experimental conditions and results

Run #	T °C	P_{in} MPa	P_f MPa	t mn	u m/s	Stable phases	Seeds Plag d_{plag} µm	Ol d_{ol} µm
Decompression								
R16-1	1180 → 1150	250	50	499.5	0.26	L, Cpx, Ol	-	-
R16-2	1180 → 1150	250	50	499.5	0.26	L	-	-
Interaction								
R6-1[a]	1150	28	28	115	-	L, Ol	-	10-20
R6-2	1150	28	28	115	-	L, Ol	33	-
R7-1[a]	1150	194	194	11	-	L	-	10-15
R7-2	1150	194	194	11	-	L, Cpx, Ol	18	-
R9-1[a]	1150	25	25	15	-	L, Ol	-	5
R9-2	1150	25	25	15	-	L, Ol	7	-
R9-4[b]	1150	25	25	15	-	L, Ol	-	5
R2-7[a]	1150	199	49	152	0.63	L	-	150-250
R2-8	1150	199	49	152	0.63	L	65	-
R4-4[a]	1150	200	48	95	1.03	L	-	100-150
R4-5	1150	200	48	95	1.03	L	79	-
R5-3[a]	1150	201	25	110	1.02	L	-	100-150
R5-4	1150	201	25	110	1.02	L	46	-
R10-3[a]	1150	198	25	173	0.64	L	-	200-300
R10-6[b]	1150	198	25	173	0.64	L	-	200-300

T: run temperature; P_{in}: pressure at the beginning of decompression ramp, P_{fin}: pressure at the end of decompression ramp; for isobaric experiments, $P_{in} = P_f$; u: ascent/decompression rate (= 10^6 (P_{in} - P_{fin}) / (g d t)), with g = 9.81 m / s^2, d = 2650 kg / m^3 and t = duration of the ramp.
R16-1 and R16-2 were ran in the same experiment but with two different LP-type starting glasses. See Pichavant et al. (2013). Note that the experiment is non-isothermal. Temperature varied approximatively linearly along the decompression path.
Stable phases include L: silicate melt (quenched to glass), Cpx: clinopyroxene, Ol: olivine.
[a]Stromboli and San Carlos olivine seeds placed together with glass in the same capsule; [b]Stromboli olivine seed alone with glass. For all other charges plagioclase seed loaded together with glass. Plagioclase (Plag) and olivine (Ol) seeds remain present in all interaction charges and d_{plag} and d_{ol} are widths of the plagioclase and olivine reaction zones respectively, measured on SEM images.

Table 3. Textural characteristics of samples

Paroxysm	Sample	Volume mm^3	n	D µm	D_{av} µm	N_v mm^{-3}	V vol%	Exponent
August 2019	PST 2019-8	102	97653	12-1141	36 (21)	8196 (1052)	86 (1)	1.00
July 2019	PST 2019-1	11	9402	12-630	55 (46)	2889 (391)	70 (3)	1.44
	PST 2019-4	42	30670	12-928	76 (40)	3503 (847)	77 (4)	1.25
March 2007	Polacci et al. (2009)		1.6	-	-	860	58	1.40
April 2003	Polacci et al. (2009)		15.7	-	145-161	643	57	1.40
1930	PST 217	4	6265	12-393	56 (41)	8075 (1754)	78 (3)	1.12
Undated	PST-9	16	14547	12-642	73 (41)	2994 (525)	68 (4)	1.30
16^{th} century	PST 12LP	20	2047	15-840	94 (82)	720 (159)	49 (2)	
	PST 12LP	5	2688	12-508	59 (54)	1838 (445)	69 (5)	1.38

Volume: volume of the analysed sample; n: number of vesicles counted; D: range of vesicle diameters; D_{av}: average vesicle diameter; N_v: vesicle number density per unit volume of melt; V: vesicularity (% volume of vesicles in the analysed sample volume). Exponent: exponent of the power law regression of the cumulative vesicle volume distribution (bubble volumes between ~10^4 and ~10^8 μm^3, Fig. 9).

FigureS1


Click here to access/download
Supplementary Material
FigS1.eps

FigureS2


Click here to access/download
Supplementary Material
FigS2.eps

FigureS3


Click here to access/download
Supplementary Material
FigS3.eps

FigureS4


Click here to access/download
Supplementary Material
FigS4.eps

FigureS5

FigureS6


Click here to access/download
Supplementary Material
FigS6.eps

FigureS7


Click here to access/download
Supplementary Material
FigS7.eps

TableS1

TableS2

TableS3

TableS4


Click here to access/download
Supplementary Material
TableS4.pdf

TableS5

TableS6